

DISCLAIMER FOR FRONT PAGE OF MATERIALS TO BE MADE AVAILABLE VIA ETI INTERNET SITE

1. "Save to the extent set out in paragraph 2 below, this document and its contents are made available to you via the ETI's Internet Site "as is" without any representations, conditions, warranties or other assurance of any kind. The ETI and the authors, together with their employees, directors, servants or agents exclude to the maximum extent permissible by law all representations, warranties, conditions or other assurance whatsoever (whether express or implied) regarding the use of this document or its content including any warranties of title, merchantability, accuracy, completeness, non-infringement or that the document or its contents are of satisfactory or any particular quality or fit for any particular purpose. Any person accessing this document and using it or any of its contents accepts all risk in doing so.
2. Notwithstanding any statement to the contrary contained on the face of this document, the ETI confirms that the authors of the document have consented to its publication by the ETI."



Energy Technologies Institute

PerAWaT

WG3 WP1 D3: PERFORMANCE AND WAKE STRUCTURE OF A MODEL HORIZONTAL AXIS AXIAL FLOW TURBINE

Authors S. C. McIntosh, C. F. Fleming, R.H.J. Willden

Version 2.0

Date 19/12/12

Revision History		
Issue / Version	Issue Date	Summary
0.1	08/12/11	First draft for review by GH
1.0	09/12/11	Resubmitted following feedback from GH
1.1	11/12/12	Report updated to include comparison to EDF's full experimental data-set

2.0	19/12/12	Report re-submitted following feedback from GH
-----	----------	--

1 Executive Summary

The report details simulations of a model scale three-bladed axial flow tidal turbine operating in sheared flow. The simulations are based on the series of experiments carried out thus far by EDF as part of the PerAWaT project (WG4 WP1 D4), where velocity and bed roughness parameters are modified to produce a range of flow conditions.

The rotor is modelled through both the blade-resolved and RANS-BEM methods. Rigid lid and volume-of-fluid (VOF) free surface approximations are employed.

Good agreement is observed for standard rotor performance coefficients, and fair agreement is attained for velocity profiles extracted from the turbine wake under various operating conditions, validating the numerical approaches and models.

A full matrix of simulations is tabulated, with the results of a selection of these presented in detail and compared to corresponding EDF data. The full database of simulation results is available for download from the PerAWaT sftp server.

Table of contents

1	Executive Summary	1
1	Introduction	4
2	Methodology.....	6
2.1	Model Geometry	6
2.1.1	Rotor	6
2.1.2	Channel Geometry	8
2.2	Mesh generation.....	10
2.2.1	Sliding mesh interface	10
2.2.2	Rotor mesh.....	11
2.2.3	Meshing methods.....	13
2.3	Free Surface Tracking	16
2.4	Wall Roughness Modelling	17
2.5	Computational Cost	18
3	Results.....	19
3.1	General.....	19
3.2	Empty flume velocity profiles.....	21
3.3	Results Overview.....	24
3.3.1	Power and thrust.....	24
3.3.2	Sheared flow	26
3.4	Near Wake	29
3.5	Wake Profiles	32
3.5.1	Low flow velocity – low turbulence intensity (U0T0)...	Error! Bookmark not defined.
3.5.2	Low flow velocity – high turbulence intensity (U0T1) .	Error! Bookmark not defined.
4	Conclusions.....	33
5	References	35
6	Appendix	36
6.1	Low Velocity – Low Shear (U0T0)	36
6.1.1	Centreline Velocity Profile	36

6.1.2	Horizontal Velocity Profiles	37
6.1.3	Vertical Velocity Profiles	40
6.1.4	Velocity Grids	42
6.2	Low Velocity – High Shear (U0T1)	44
6.2.1	Centreline Velocity Profile	44
6.2.2	Horizontal Velocity Profiles	45
6.2.3	Vertical Velocity Profiles	48
6.2.4	Velocity Grids	50
6.3	High Velocity – Low Shear (U1T0)	52
6.3.1	Centreline Velocity Profile	52
6.3.2	Horizontal Velocity Profiles	53
6.3.3	Vertical Velocity Profiles	54

1 Introduction

This report forms Deliverable D3 of Work Group 3 Work Package 1 of the PerAWaT project. The current deliverable follows on from an interim deliverable WG3WP1D3 v1.0, now comprising a full comparison to a broad experimental campaign being carried out by Électricité de France (EDF), a PerAWaT partner, on a 1/30th scale model axial flow tidal turbine.. The work in this deliverable, carried out at the University of Oxford, involves Computational Fluid Dynamics (CFD) simulation of an axial-flow tidal turbine at model scale.

Model validity, as well as capability to replicate complementary experimental work, is demonstrated. The report describes model structure and functioning, including all assumptions and algorithms.

Section 2.1 gives geometrical details of the numerical model. The channel dimensions correspond to the EDF flume, and the rotor geometry is taken from Computer-Aided Design (CAD) designs provided by the PerAWaT consortium.

The rotor is modelled using two techniques; blade resolved CFD and RANS embedded BEM modelling, which have been discussed in detail in Deliverables D1 and D2 of this Work Package. The RANS-BEM method is a steady solution method in which the presence of the blades at the rotor plane are represented in a time average sense through blade forces evaluated according to the local flow and prescribed force coefficient variations. The method is effective in predicting turbine performance in terms of power and thrust coefficients, without a large computational overhead. If a time averaged steady flow solution is not sufficient then localised flow features, e.g. vortex structures generated by discrete blades, can be simulated and analysed through the computationally-intensive blade-resolved rotor model.

The relevant domains, a rectangular cross-section flume in the case of RANS-BEM and the same with an inner rotating coin to contain the moving rotor in the case of blade resolved CFD, are discretised using an unstructured meshing algorithm. The algorithm provides a robust approach to capture complex

geometries; further details are provided in Section 2.2.

The physical experiments are conducted in an open channel and as such the free surface must deform to accommodate energy removal from the flow. Numerically the free surface can be modelled either as a deforming surface, or, if height change is small relative to depth, as a rigid lid. Details of the models employed in the numerical simulations are provided in Section 2.3.

A phenomenon commonly observed in RANS turbulence modelling is the unintended decay of free-stream turbulence with streamwise distance from the inlet boundary. This is a natural decay process and is a consequence of a lack of wall shear that would otherwise naturally act to reinforce the profile and free-stream turbulence in a real flow. Such decay can be reduced through specifying a sheared profile of mean flow velocity at the inlet boundary, and maintaining this profile through the application of wall shear at the floor and sides of the channel. A wall function has been developed to apply appropriate wall shear to achieve velocity and turbulence intensity profiles corresponding to those observed in the EDF experiments. Details are given in Section 2.4.

Employment of the RANS-BEM rotor model in addition to the blade-resolved model enables the exploration of a wide set of model parameters. Results from both numerical methods are presented in Section 3 starting with an outline of the simulation matrix in Section 3.1. An overview of the performance metrics, power and thrust, of the five flow cases, combinations of flow velocity and turbulence levels, are presented in Section 3.2, including comparison where possible to comparable metrics from the EDF experiments. Section 3.3 presents wake details for a single flow case.

Discussions concerning the validity of both RANS-BEM and blade resolved simulation methods are presented in Section 3.3. The report concludes with an extensive comparison of computational and experimental wake data. This forms a substantial data set which has been placed in an appendix at the end of this report.

2 Methodology

The objectives of this deliverable are to a) simulate the operation of an axial flow turbine in an open channel via a Reynolds Averaged Navier Stokes (RANS) solver, b) to compare the numerical simulation results to experimental data, and c) to hence validate the numerical model. The turbine under examination is the three-bladed model designed within the PerAWaT project (Whelan, 2010). The computational model aims to emulate as closely as possible the physical experiments that are being conducted by EDF. Simulations are carried out for a series of flow cases where the inflow velocity and turbulence intensity are altered. A database of simulation results is produced for comparison to the experimental results. Various aspects of the computational model are described below.

2.1 Model Geometry

2.1.1 Rotor

Two rotor modelling techniques are employed; the RANS-BEM method and the blade-resolved method. Details of these rotor models are given in Deliverable D2 of this Work Package (Fleming et al., 2011). The computationally lightweight RANS-BEM method is used in the development stages, where the focus is on the wall shear and free-surface tracking models. Additionally, the RANS-BEM method has proven to yield accurate predictions of rotor power and thrust, and hence these simulations may be used to complement a smaller number of computationally demanding blade-resolved simulations. Hence a wide parameter survey becomes possible, as demonstrated in Section 3.1. By contrast the finiteness of computational resources necessitate that the more demand blade-resolved simulations are carried out at a limited number of operating points for each flow case.

The geometry of the rotor, nacelle, and tower has been provided by PerAWaT project partners both in CAD and tabulated data formats (Whelan, 2010). The

intention of the rotor design was to thrust match experiments being conducted elsewhere in the project at various scales. However, on detailed examination of the specified rotor geometry and that drawn in the CAD file major differences became apparent. Oxford performed a deconstruction of the CAD geometry to yield the chord and geometric twist distributions shown in the figures below, in which “Excel” refers to the specified geometry, and “CAD” to that drawn in the CAD files.

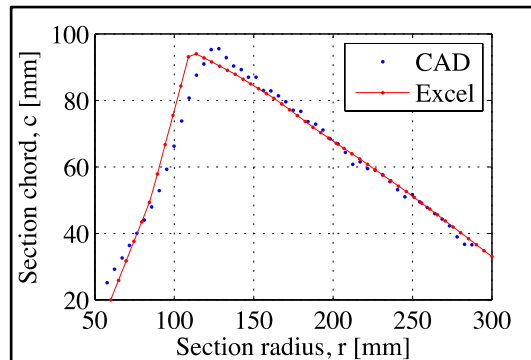


Figure 2.1-1: Blade chord distribution.

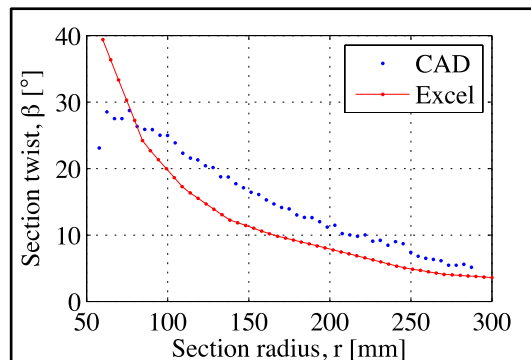


Figure 2.1-2: Blade twist distribution.

It is clear that the major differences arise in the twist distribution. For the most part the CAD rotor blades have increased twist of between 2° and 7° over that specified in the tabulated Excel specification, although the inboard CAD section is less twisted relative to specification.

It has been presumed that the physical rotor under test at EDF has been built according to the CAD files. It has been confirmed by EDF that there is no additional root pitch mechanism on the rotor blades so that the rotor is presumed to operate as drawn in the CAD files. Hence, as the objective of this

work package is to validate the numerical models, the CAD rotor geometry has been used as the basis for the numerical turbine.

2.1.2 Channel Geometry

The channel cross-section is presented in Figure 2.1-3, with the outline of the rotor shown indicated by a broken line.

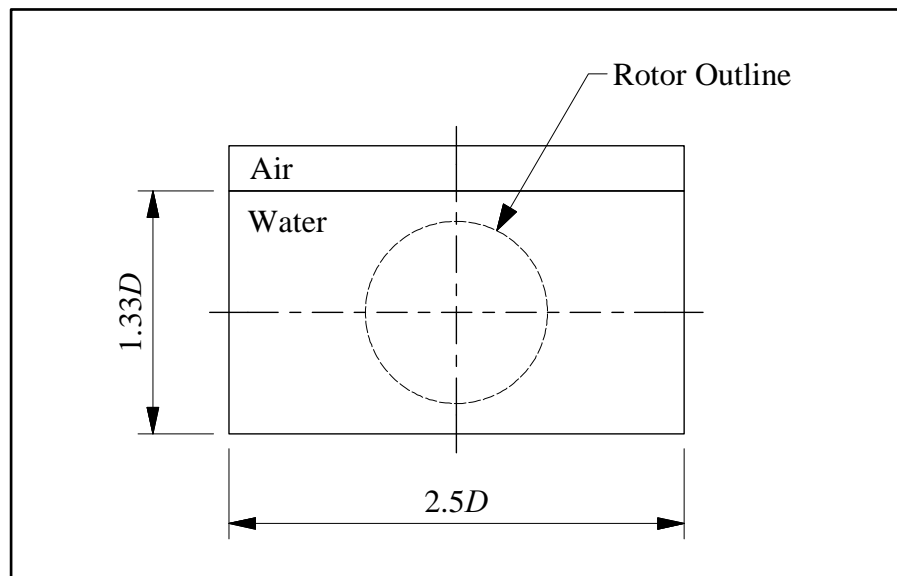


Figure 2.1-3: Cross-section through channel.

The majority of the simulations are carried out on a channel with a distance to the upstream boundary of three rotor diameters, D , and a downstream distance of six rotor diameters, following on from previous work in this Work Package (McIntosh et al., 2010; Fleming et al., 2011). For a selection of cases, the development of the far wake is tracked for a distance of forty diameters downstream of the rotor. An elevation view of the short channel is shown in Figure 2.1-4.

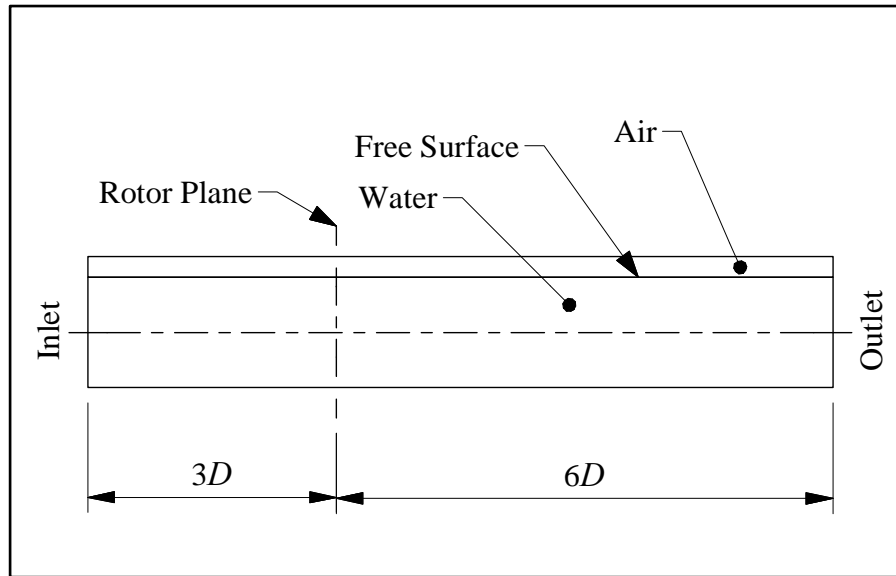


Figure 2.1-4: Elevation view of short 3-6D channel.

The major dimensions of the model are summarised in Table 2.1.1.

Part	Dimension	Meters, m	Rotor diameters, D
Rotor	Diameter, D	0.6	1
	Centreline elevation	0.4	0.66
Channel	Water depth	0.8	1.33
	Width	1.5	2.5
	Upstream length	1.8	3
	Downstream length (short)	3.6	6
	Downstream length (long)	24	40

Table 2.1.1: Principal dimensions of the model.

2.2 Mesh generation

2.2.1 Sliding mesh interface

The rotor and spinner are enclosed within a cylindrical region, which behaves as a sliding mesh interface, allowing relative motion between the rotor and the channel (see Figure 2.2-1). The interface boundary is lined with non-conformal meshes of two-dimensional triangular elements on the interior and exterior surfaces respectively. Surface elements on this boundary are constrained to be of constant size, in order to reduce interpolation errors in computed fluid variables passed between neighbouring volumes across the sliding interface.

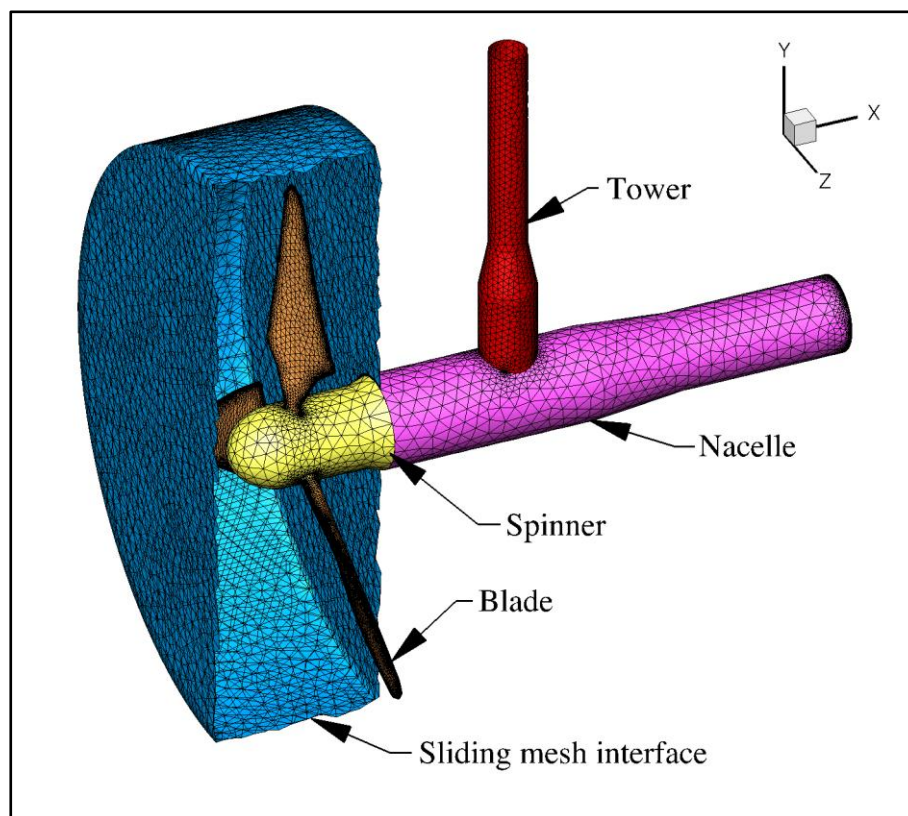
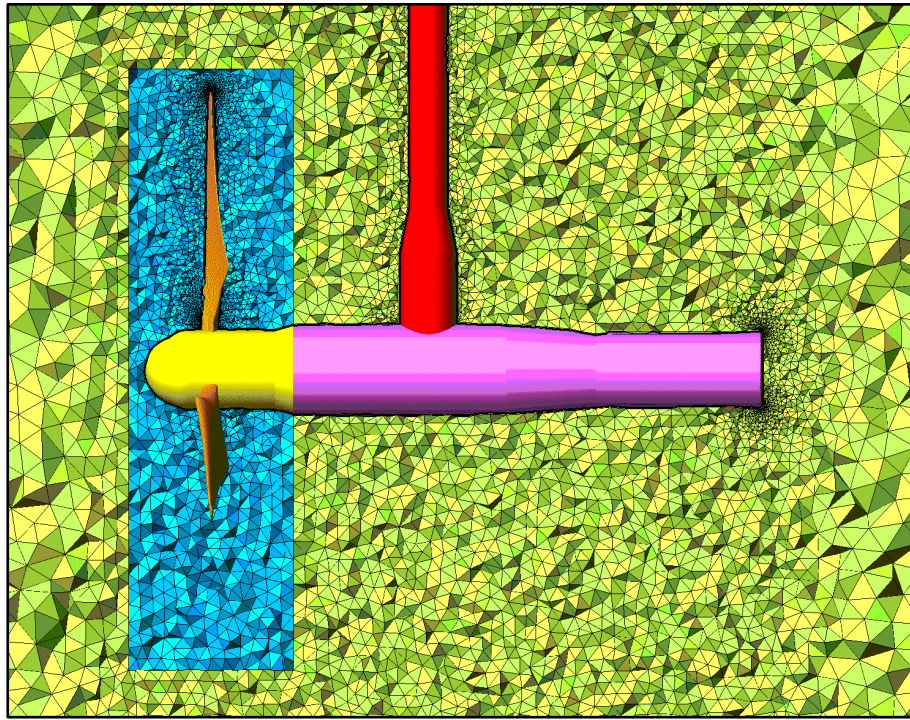


Figure 2.2-1: Three-dimensional view of the surface mesh of triangular elements on the blade-resolved rotor model. Two non-conformal layers of surface elements are visible on the sliding mesh interface. All of the volume and surface elements within the sliding mesh region revolve, while the external mesh remains stationary.

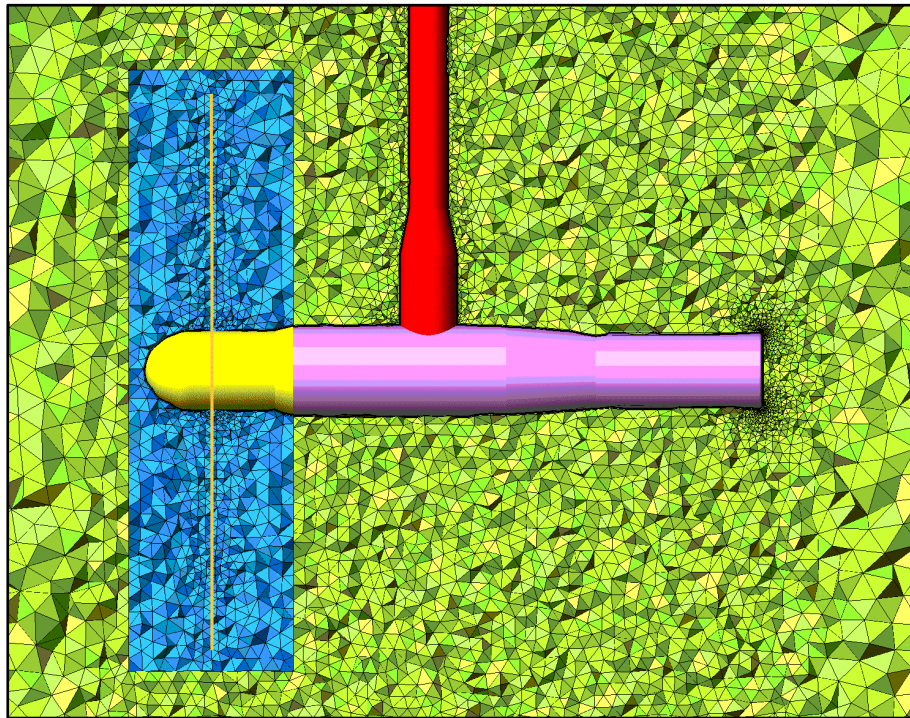
2.2.2 Rotor mesh

The mesh is generated in a modular process. The interior (rotor) and exterior (channel) volume meshes are generated separately. The non-conformal interface is created by merging a rotor and a channel mesh together.

Although not strictly required, the same modular approach is taken in generating meshes for the RANS-BEM model. Hence, in comparisons between the two rotor models, the respective far-field meshes are identical. An illustration of the two meshes is presented in Figure 2.2-2. In addition, the near field regions in each case have the same limit on maximum tetrahedral element size.



(a)



(b)

Figure 2.2-2: Comparison of near field and far field meshes for (a) the blade-resolved rotor model and (b) the RANS-BEM rotor model. The far field mesh regions (green) are identical, while the near field regions (blue) have the same limit on maximum element dimension.

2.2.3 Meshing methods

Each mesh is generated in three successive stages, where the surface elements, volume elements, and boundary layer elements are created.

a) Surface mesh

The surface mesh, which consists solely of triangular elements, is computed using the robust Octree algorithm. Initially, maximum triangular element dimensions are specified on each surface. The fluid volume is then temporarily filled with tetrahedral elements of a specified size, each of which may be subdivided to produce eight smaller elements. This subdivision is repeated successively near geometrical surfaces in order to achieve the required maximum triangular element size at that surface. Further subdivision then occurs to capture surface curvature adequately. The tetrahedral elements are then removed to leave a surface mesh, as shown in Figure 2.2-1 above.

b) Volume mesh

In previous work by the authors (McIntosh et al., 2010; Fleming et al., 2011), the tetrahedral elements produced by the Octree algorithm were retained. The resulting mesh features sudden step changes in volume, generally by a factor of two, between neighbouring elements (see Figure 2.2-3(a)). Such transitions in element volume are undesirable in a finite volume solver, as solution convergence rate may be hindered.

Gradual and controlled transitions in element volume may be achieved by the Delaunay algorithm. Beginning with a mesh consisting solely of two-dimensional triangular surface elements, layers of tetrahedral elements are grown from the surface elements, with the elements of subsequent layers increasing in volume by a constant ratio, until the domain is filled. Limits on the maximum dimension of tetrahedral elements may be specified throughout the volume. The resulting volume mesh is demonstrated in Figure 2.2-3(b).

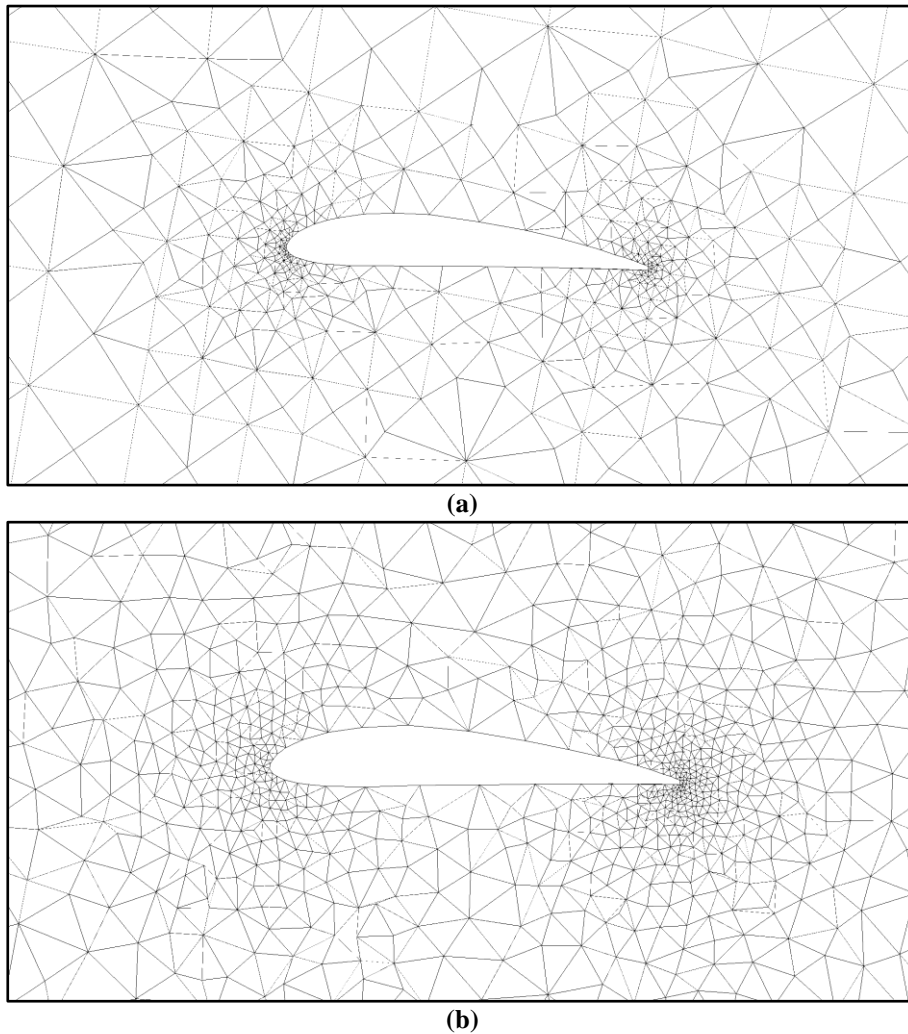


Figure 2.2-3: Comparison of (a) the Octree and (b) the Delaunay mesh generation algorithms, showing a projection of the tetrahedral volume mesh onto a cutplane through the rotor blade at the 80% radial station.

The use of the Delaunay meshing technique grown from the Octree surface mesh results in smoother volume changes through the mesh, improved mesh quality and improved numerical stability characteristics.

c) Boundary layer mesh

The boundary layer flows adjacent to the rotor and support structure geometry require very high mesh resolution in the wall-normal direction. This is achieved in the conventional manner by substituting layers of high aspect ratio prismatic elements for the tetrahedral elements on these surfaces. In order to explicitly resolve a boundary layer, the centroid height of the wall adjacent cells

must be such that a dimensionless wall distance, $y^+ = y/\nu\sqrt{\tau_w/\rho}$, of less than 1.0 is achieved (where τ_w is the wall shear stress, y the normal distance from the wall, ν and ρ the kinematic viscosity and density respectively). The appropriate centroid height is determined through an iterative series of simulations of flow conditions around a blade section corresponding to maximum torque production. These conditions occur at the 80% radial station of the blade, where the local flow Reynolds number is approximately 42,000 (based on blade chord) and the local angle of attack, α , is 6.6° . Work carried out earlier in the project (McIntosh et al., 2010) has shown that a wall-adjacent cell centroid height of 5×10^{-6} m is required.

The boundary layers on the blade, spinner, nacelle and tower surfaces are resolved with twelve layers of prismatic elements, with a first layer centroid height of 5×10^{-6} m and a growth ratio of 1.5. Reasonably good transitions in volume are achieved between the upper layer of prism elements and the adjacent tetrahedral elements, as shown in Figure 2.2-4 and Figure 2.2-5.

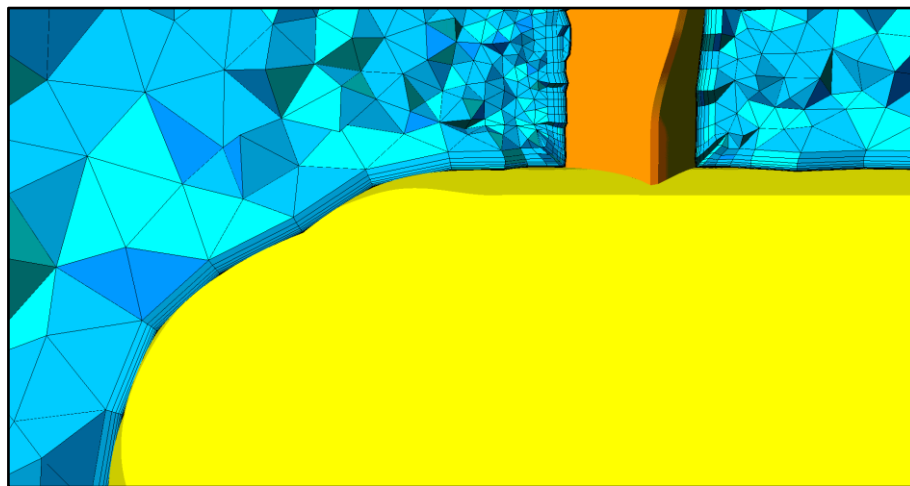


Figure 2.2-4: Elevation view of a cutplane through the volume mesh adjacent to the spinner (yellow) and blade (orange). Layers of prismatic elements are used to resolve the boundary layers at the blade and spinner surfaces, while the rest of the volume is occupied by tetrahedral elements.

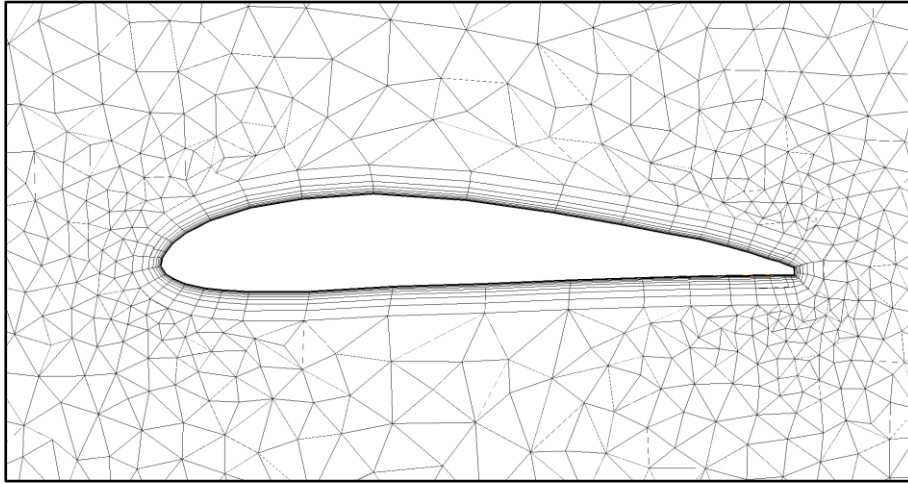


Figure 2.2-5: Outline of volume mesh elements projected onto a cutplane perpendicular to blade at 80% radial station.

2.3 Free Surface Tracking

The flow is expected to undergo a small drop in free surface elevation as momentum is transferred to the turbine. The Volume of Fluid (VOF) method is used to track the free surface deformation (McIntosh et al., 2010). As the energy removal from the system cannot be specified a priori, the height of flow at the downstream boundary cannot be set explicitly but is a product of the simulation. An iterative technique is employed to adjust the downstream boundary height so as to achieve, for a prescribed upstream Froude number, uninhibited energy removal by the turbine and ensuing wake mixing, with no spurious energy sinks or sources in the flow to account for boundary induced energy conservation errors. Further details of this technique can be found in (McIntosh et al., 2010).

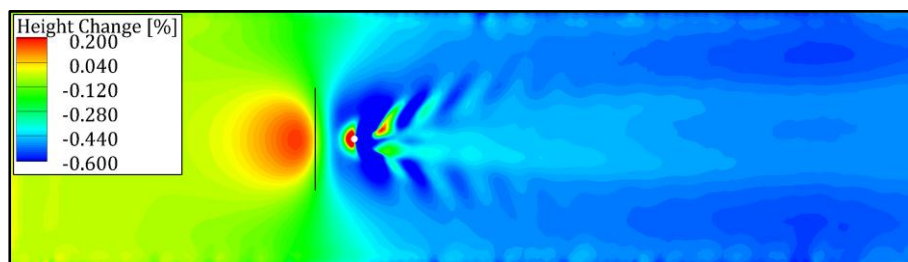


Figure 2.3-1: Plan view of channel with contours of free surface deformation. Flow direction is from left to right, and the rotor location is highlighted with a black line. Flow case U1 T0, $\lambda = 4$.

While reasonably large local free surface deformation occurs near the tower (see Figure 2.3-1), the overall reduction in free surface elevation is small ($\sim 0.5\%$). As such the free surface may be adequately approximated as a non-deforming free surface, i.e. as a rigid lid. This approximation has been shown to be valid up to very high blockage ratios (Consul et al., 2011); 50% flow blockage by area was shown to yield differences in power and thrust coefficients of a few percent between calculations with a rigid lid and those with a deformable free surface.

2.4 Wall Roughness Modelling

Analysis on the base flow of the EDF flume has shown that it is highly turbulent, with significantly sheared profiles of velocity and turbulence intensity (McIntosh et al. 2010). These sheared profiles are reproduced in a RANS simulation by setting an appropriate wall roughness height at the bed and walls of the channel (McIntosh et al., 2010).

Application of the appropriate level of shear at the domain boundaries required to achieve the high shear-turbulence state recorded in the EDF flume, leads to reversed flow occurring in the wall-adjacent cells. Although non-physical, this phenomenon only occurs adjacent to the channel bed and walls, and is necessary to produce the correct sheared velocity profile. However, reversed flow anywhere on the outlet boundary hinders solution convergence. The wall shear model is therefore deactivated a short distance upstream of the channel outlet to allow the reversed flow near the channel walls to recover.

The shear model is shown to preserve the velocity profile prescribed at the inflow, as shown in the figures in Section 3.2 below.

2.5 Computational Cost

The total element count of the various meshes employed is outlined in the table below. Note that the VOF air domain extension is only used with the short domain model.

Rotor Model	Short Domain	Long Domain
BEM	3.14M	9.86M
Blade Resolved	4.92M	n/a
VOF	additional 0.59M	n/a

Table 2.5.1: Element count in each simulation model (Millions).

For the short domain, rigid lid computations, the RANS-BEM simulations take approximately 12 CPU-hours noting that these are steady flow simulations, whilst the blade resolved simulations require circa 100 CPU-hours per turbine revolution.

3 Results

3.1 General

A considerable number of model parameters are available for examination; as listed in Table 3.1.3. The simulation series are identified serially in the first column. Results of further simulations, not presented here, are available online from the PerAWaT sftp site. Three velocity levels and two bed roughness levels are examined; see Tables 3.1.1 and 3.1.2. The velocity is measured at a point directly upstream of the axis of revolution of the rotor, i.e. at hub height.

Velocity Level	Velocity (m s ⁻¹)
U0	0.27
U0.5	0.41
U1	0.55

Table 3.1.1: Velocity levels and corresponding hub height velocities.

Turbulence Level	Velocity Level	Roughness Height [m]
T0	U0	6.12×10^{-5}
T1	U0	1.44×10^{-2}
T0	U0.5	1.42×10^{-4}
T0	U1	3.31×10^{-3}
T1	U1	6.48×10^{-3}

Table 3.1.2: Turbulence levels and corresponding wall roughness heights.

Series	Tip Speed Ratio, λ	Velocity			Turbulence		Rotor Model		Free Surface		Channel		Shear		
		U0	U0.5	U1	T0	T1	Blade Resolved	RANS-BEM	RL	VOF	Short	Long	Bed & Walls	Bed	None
1	N/A	•			•		N/A		•		•		•		
2			•		•		N/A		•		•		•		
3				•	•		N/A		•		•		•		
4		•				•	N/A		•		•		•		
5				•		•	N/A		•		•		•		
6	3-5	•			•		•		•		•		•		
7			•		•		•		•		•		•		
8				•	•		•		•		•		•		
9		•				•	•		•		•		•		
10				•		•	•		•		•		•		
11	1-8	•			•			•	•		•		•		
12			•		•			•	•		•		•		
13				•	•			•	•		•		•		
14		•				•		•	•		•		•		
15				•		•		•	•		•		•		
16		•			N/A			•	•		•				•
17		•			•			•	•		•			•	
18 (as 11)		•			•			•	•		•		•		
19		•				•		•	•		•			•	
20 (as 14)		•				•		•	•		•		•		
21				•	N/A			•	•		•				•
22				•	•			•	•		•			•	
23 (as 13)				•	•			•	•		•		•		
24				•		•		•	•		•			•	
25 (as 15)				•		•		•	•		•		•		
26	1-8	•			•			•		•	•		•		
27			•		•			•		•	•		•		
28				•	•			•		•	•		•		
29		•				•		•		•	•		•		
30				•		•		•		•	•		•		
31	4	•			•			•	•			•	•		
32			•		•			•	•			•	•		
33				•	•			•	•			•	•		
34		•				•		•	•			•	•		
35				•		•		•	•			•	•		
36		•			N/A			•	•			•			•
37		•			•			•	•			•		•	
38 (as 31)		•			•			•	•			•	•		
39		•				•		•	•			•		•	
40 (as 34)		•				•		•	•			•	•		

Not to be disclosed other than in line with the technology contract

41		•	N/A	•	•	•	•
42		•	•	•	•	•	•
43 (as 33)		•	•	•	•	•	•
44		•	•	•	•	•	•
45 (as 35)		•	•	•	•	•	•

Table 3.1.3: Simulation matrix showing model parameters examined.

In the simulation matrix above series 18, 20, 23, 25, 38, 40, 43 and 45 are repeats of previous series and are repeated in the tabulation for convenience of reference. Each simulation series was run across a range of tip-speed-ratios, λ . Series 1 - 5 are base flow cases in the absence of a turbine, which are used to verify that the velocity profile is maintained. Therefore, the tip-speed-ratio and rotor model parameters are not applicable. Modelling of the free surface is indicated as either RL (Rigid Lid) or VOF (Volume-Of-Fluid, i.e. deformable). Latter investigation series examined the impact of wall and bed shear on the turbine and wake flows. Shear was applied on the Bed alone, both “Bed & Walls” or not at all as indicated in the final column of the table. In the case that no shear was applied at either bed or walls the turbulence level is low and decays from the inlet. Note that series 2, 4, and 31 - 45 are not reported in this document but are available on the sftp server.

3.2 Empty flume velocity profiles

A check on the wall shear model described in Section 2.4 is now made. Figure 3.2-1 reports vertical and cross-stream traverses of streamwise velocity for three flow conditions (cases 1, 3 and 5 in Table 3.1.3) in the empty numerical flume. As shown in the figure the wall model works well to produced a stable profile that decays little in the streamwise direction. The profile is particularly well held for the low turbulence level flow conditions, (U0, T0) and (U1, T0). In the case of the high turbulence condition (U1, T1) there is some modification to the profile with stream distance but this is noted to be greatest away from the channel centreline towards the walls and bed. Good agreement is observed in the vertical profiles of computed and experimental flows. The influence of a secondary flow instability, present in the EDF flume, is apparent in the horizontal

profiles.

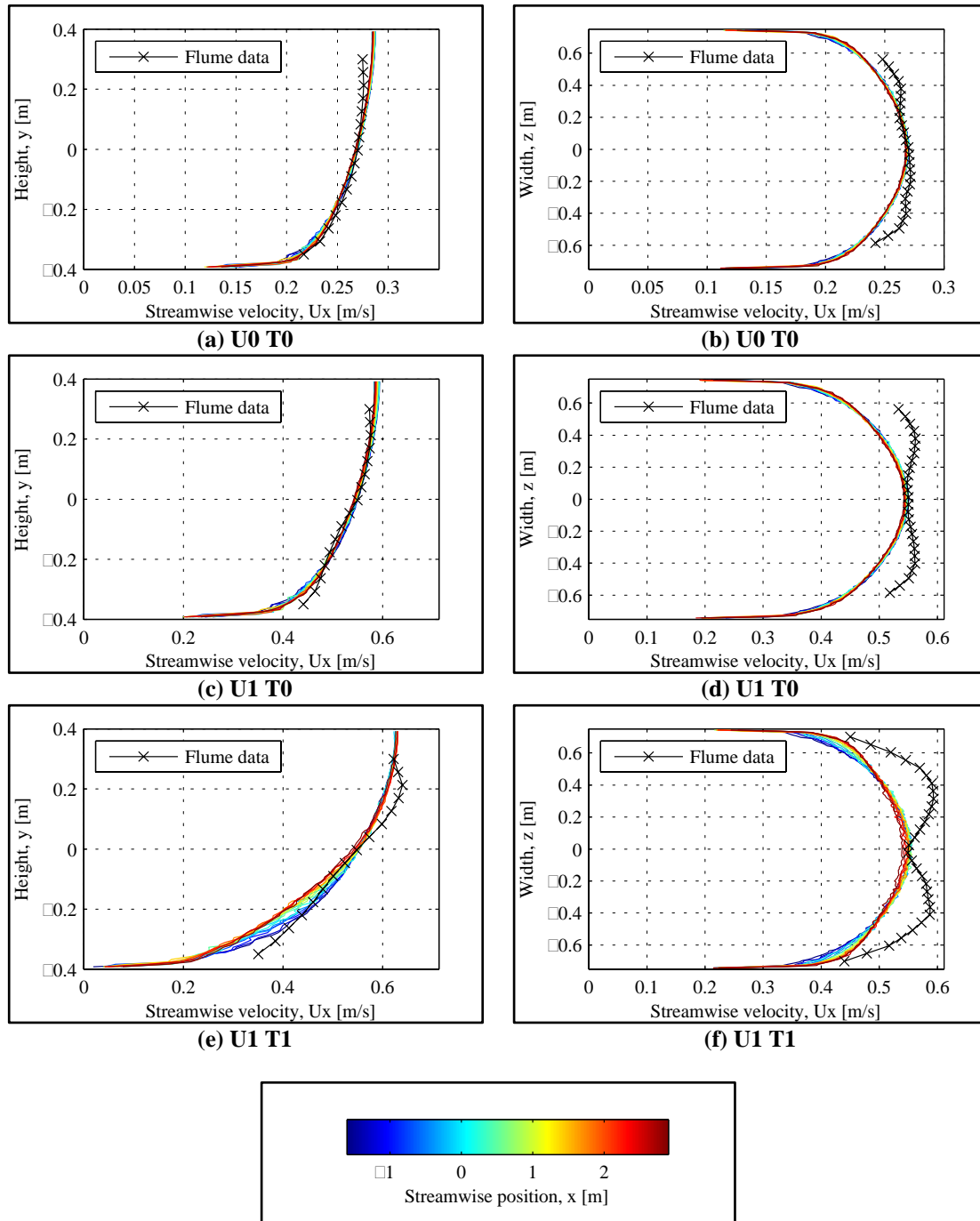


Figure 3.2-1: Centreline vertical and cross-stream profiles of streamwise velocity taken at a series of streamwise locations along the channel.

3.3 Results Overview

3.3.1 Power and thrust

In Figure 3.3-1, the results of the present simulations are compared with power and thrust coefficient measurements from the experimental in the EDF flume. Plotted are simulation results from numerical test Series 6, 7, 8 (Blade resolved with Rigid Lid), 11, 12, 13 (RANS-BEM with Rigid Lid), and 26, 27, 28 (RANS-BEM with VOF).

In all cases the alternative representations of the turbine, blade resolved and RANS-BEM, are shown to yield very similar results in terms of the performance coefficients. In comparison to the experimental data good agreement is observed for the two higher flow speed cases U0.5 and U1, although the thrust and power are under-predicted at low tip-speed-ratios. This is believed to be due to errors in prediction of blade stall at the higher angles of attack that occur at low tip-speed-ratio. The agreement with the experimental data for the lowest flow speed is less good and the reasons for this are unclear.

The effect of the free-surface modelling technique on power and thrust prediction is very slight, as can be seen by comparing the two sets of RANS-BEM results, each of which are used in combination with one of the free-surface models. Hence the decision to model the free-surface as a rigid lid in the blade-resolved simulations, taken in the interests of computational expedience, is justified.

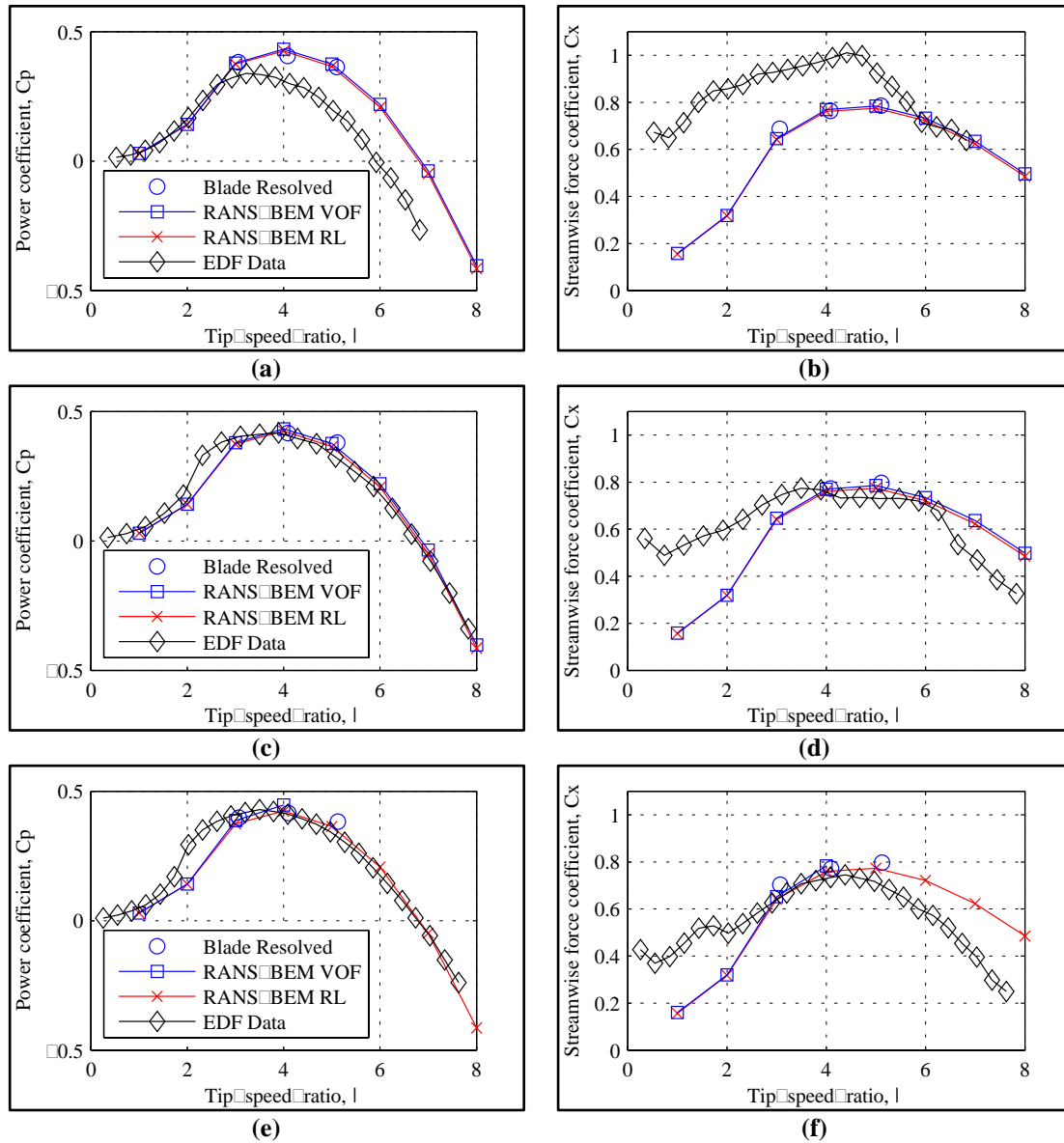


Figure 3.3-1: Comparisons of computed and measured power and thrust coefficients for a range of tip speed ratios; (a)-(b) U_0 T0, (c)-(d) $U_{0.5}$ T0, (e)-(f) U_1 T0.

3.3.2 Sheared flow

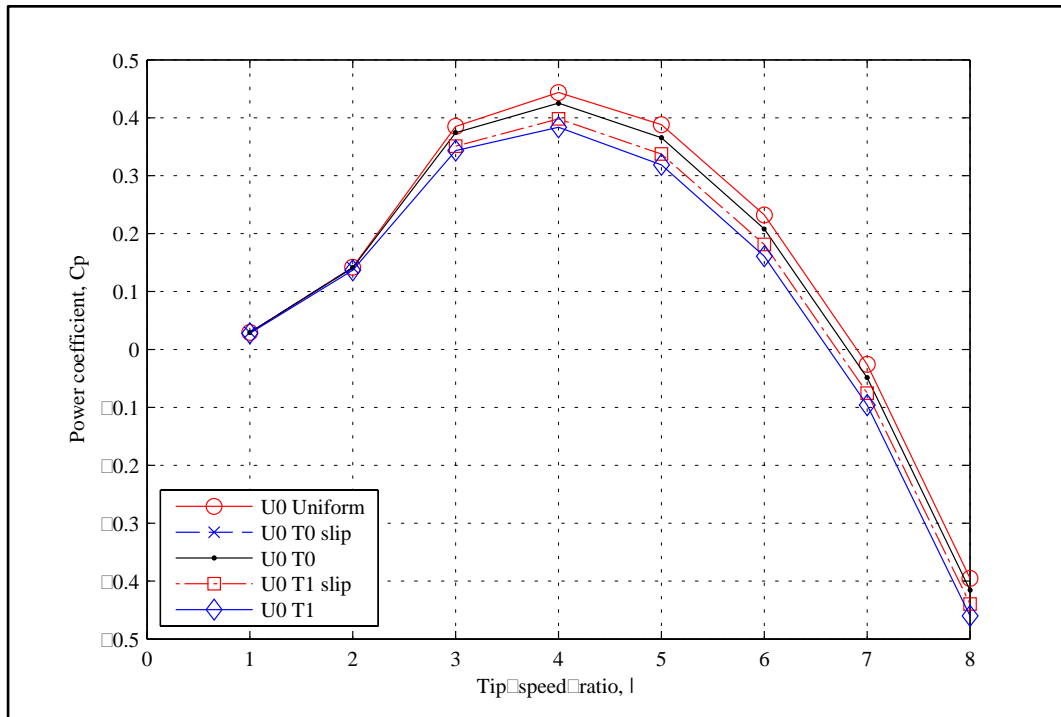
The effect of sheared flow on turbine performance is presented in Figure 3.3-2 and Figure 3.3-3 for the simulation Series 16-25 in Table 3.1.3. The flow environment of the flume differs from a real tidal flow in that it exhibits sheared profiles in both the horizontal and vertical directions, rather than in the vertical direction alone.

Initially, velocity and turbulence profiles representative of the EDF flume, i.e. which vary in the vertical and horizontal directions, are prescribed at the inflow boundary. The sheared flow profile is maintained through specification of wall shear at the bed and wall boundaries.

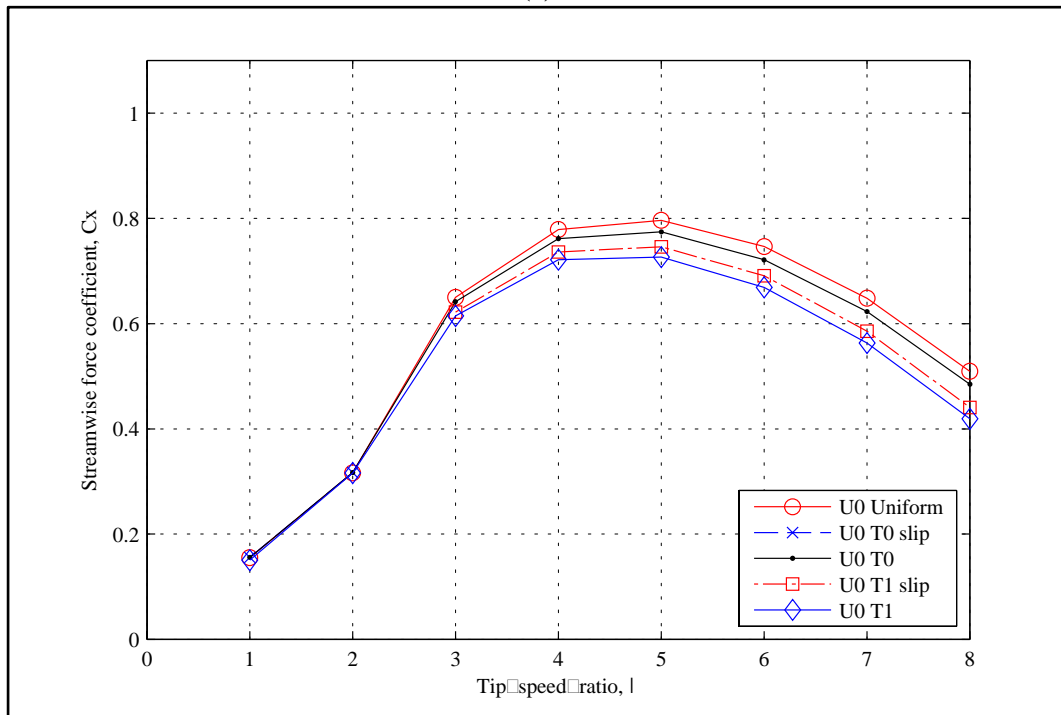
The effect of horizontal flow shear on turbine performance is examined by specifying inflow velocity turbulence profiles with vertical shear only. The shear profiles are maintained by setting an appropriate level of wall shear at the channel bed, and slip wall boundary conditions at the channel walls.

The operation of the turbine in uniform flow is examined by specifying uniform velocity and turbulence profiles at the inlet boundary, and slip wall boundary conditions at the channel bed and walls.

The flow shear is observed to reduce both the power and thrust coefficients, with a greater effect from both lateral and vertical shear than from vertical shear alone. The influence of shear is seen to be greatest for the lower velocity case.

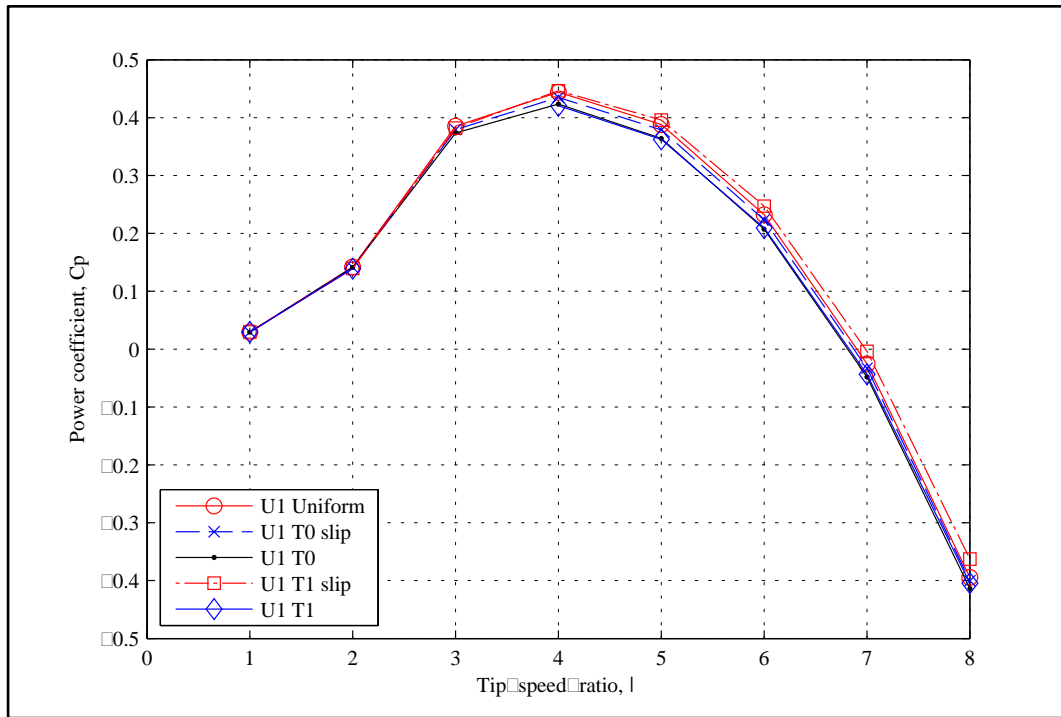


(a)

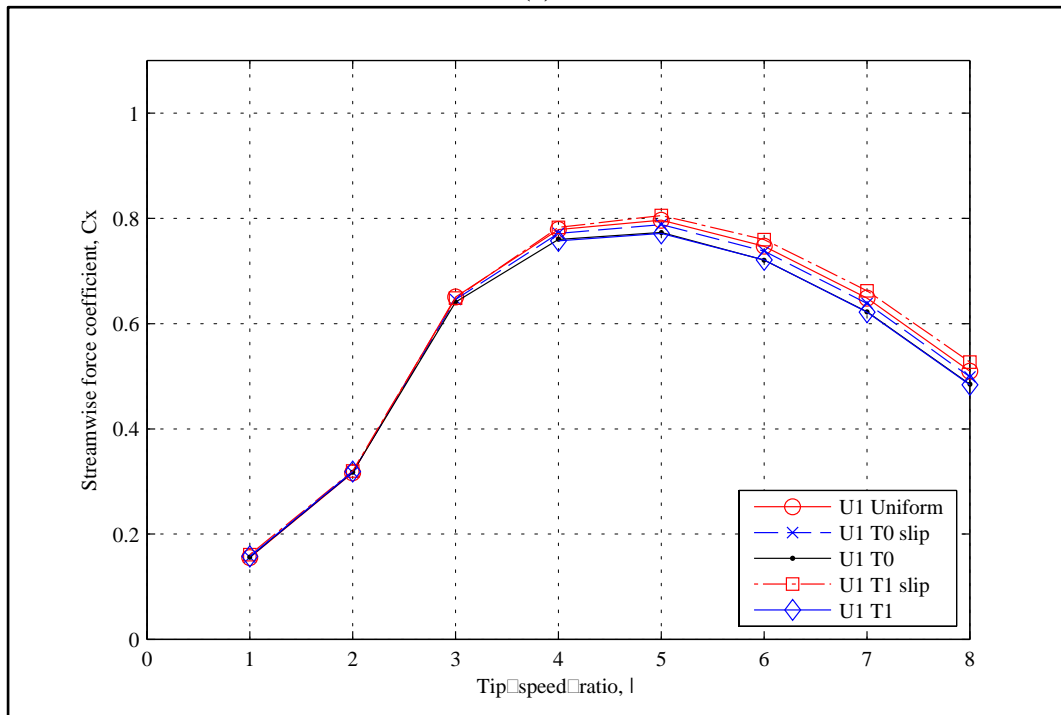


(b)

Figure 3.3-2: The effect of wall shear on (a) power and (b) streamwise force coefficients for velocity condition U0. 'U0 TX slip' refers to vertical shear only, while 'U0 TX' denotes vertical and horizontal shear. No wall shear is applied in the uniform flow case.



(a)



(b)

Figure 3.3-3: The effect of wall shear on (a) power and (b) streamwise force coefficients for velocity condition U1. 'U1 TX slip' refers to vertical shear only, while 'U1 TX' denotes vertical and horizontal shear. No wall shear is applied in the uniform flow case.

3.4 Near Wake

Comparisons of streamwise velocity along the axis of revolution of the rotor are made between experimental and computed results, RANS-BEM rotor and blade resolved (BR) with Rigid Lid in Figure 3.4-1, and RANS-BEM with VOF in Figure 3.4-2.

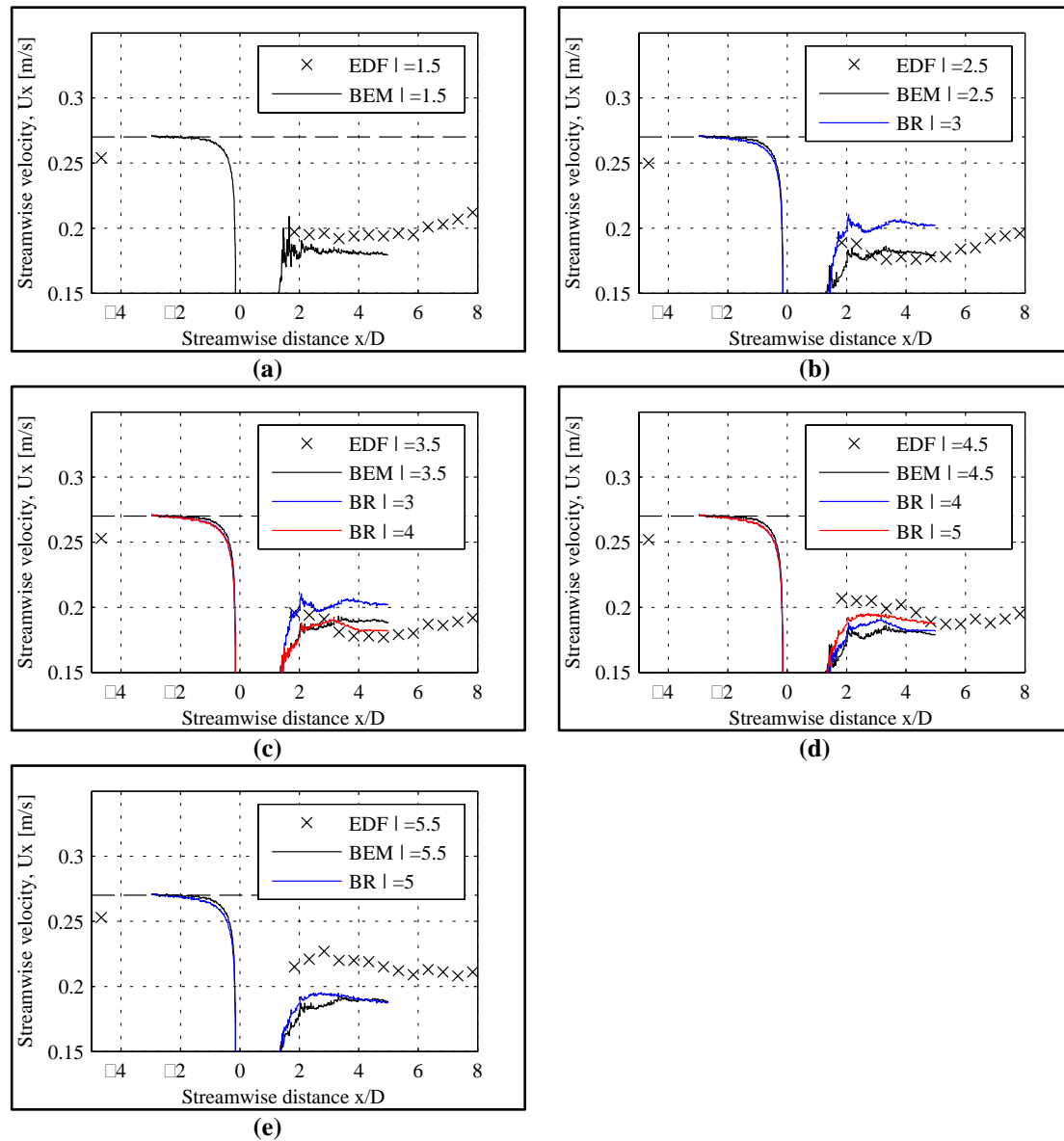


Figure 3.4-1: Profiles of streamwise velocity along the axis of revolution of the rotor. Flow Case U0 T0.

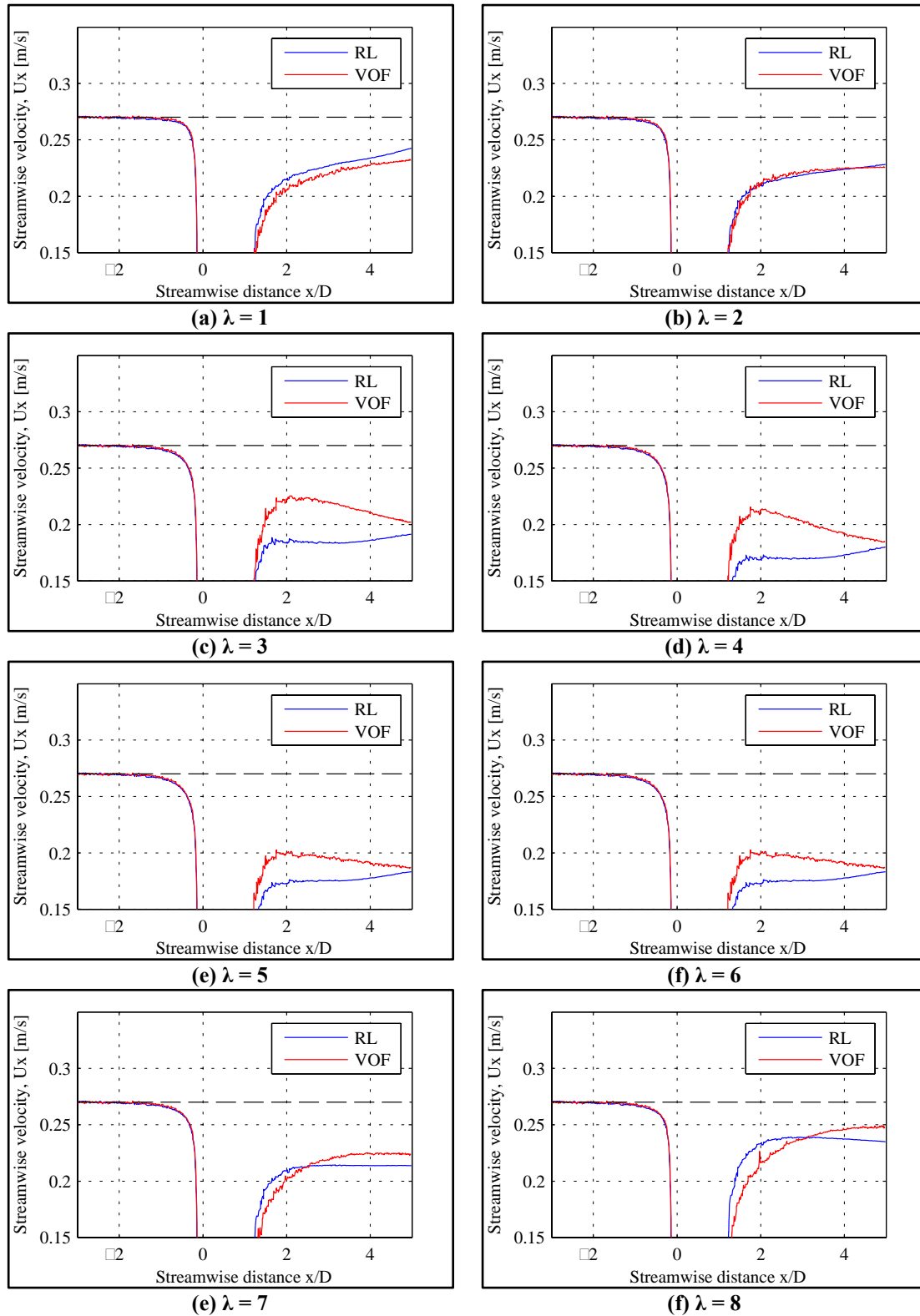


Figure 3.4-2: Profiles of streamwise velocity along the axis of revolution of the rotor. Flow Case U0 T0.

Note that experimental results are only available at integer intervals in tip-

speed-ratio between 1.5 and 5.5, whilst blade resolved data has only been computed at integer tip-speed-ratios. We observe differences in the centreline velocities aft of the turbine between rigid lid and VOF simulations commensurate with localised deformation of the free surface when the turbine is heavily loaded.

3.5 Wake Profiles

Verification of the computational model is now extended via a detailed comparison between simulated and experimental wake profiles.

Three flow cases are studied.

- I. Low flow velocity – low turbulence intensity (U0T0)
- II. Low flow velocity – high turbulence intensity (U0T1)
- III. High flow velocity – low turbulence intensity (U1T0)

For each flow case the turbine wakes are compared for five separate tip-speed-ratios ranging from $\lambda=1.5$ to $\lambda=5.5$ in equally spaced increments of $\lambda=1.0$.

The turbine wake is defined here in terms of a velocity deficit, u' .

$$u' = 1 - \frac{u}{u_{ref}} \quad (7)$$

Differences in the tip-speed-ratio matrix for the experimental ($\lambda=1.5$ to $\lambda=5.5$ in increments of $\lambda=1.0$) and computational ($\lambda=1.0$ to $\lambda=8.0$ in increments of $\lambda=1.0$) campaigns are addressed via the averaging of adjacent computational solutions for experimental tip-speed-ratio (Table 3.1.3).

Comparisons are made in the following four formats.

- I. Centreline velocity deficit
- II. Hub height horizontal profiles at six streamwise stations.
- III. Centreline vertical profiles at six streamwise stations.
- IV. A cross-stream velocity grid placed at $x=1.4\text{m}$ downstream of the rotor plane.

For the first flow case (U0T0), experimental data is available in all four formants across the five tip-speed-ratios. For the second flow case (U0T1), a reduced resolution velocity grid is employed. Whilst, for the third flow case (U1T0), no velocity grid is taken and the wakes are only recorded for two tip-speed-ratios, $\lambda=4.5$ and $\lambda=5.5$.

Comparisons for this extensive data set are laid out, as detailed above, in the

following Appendix. Direct comparisons are presented as one-dimensional plots, with experimental data represented by red crosses and the corresponding computational data by blue lines. ‘Grid-type’ comparisons are presented with a side-by-side layout for each operating tip-speed-ratio studied.

It is apparent that the numerical simulations capture the salient features of the wake; a double-dip in the vertical and horizontal profiles that is seen to recover in the stream direction. Recovery is observed to be more rapid in the experimental results, consistent with the increased mixing caused by large-scale stream-wise vortex structures observed in the flume. This effect is magnified with increasing levels of bed shear. Hence, numerical comparisons to the low shear cases (U0T0 and U1T0) are more favourable than the high shear case (U0T1).

A detailed analysis of each facet of this extensive data set is impractical. As such a subset of relevant comparisons are reported where appropriate in the appendix.

4 Conclusions

Numerical simulations of a model scale tidal turbine are carried out in sheared flow conditions using blade-resolved and RANS-BEM rotor models. The simulations are based on a campaign of model scale tidal turbine experiments carried out by EDF as part of the PerAWaT project (WG4 WP1 D4). In these experiments, a variety of flow conditions are examined, where velocity (U0, U0.5, U1) and bed roughness (T0, T1) parameters are modified. Additional numerical tests are performed to investigate the influence of horizontal shear.

During the preparation of the current simulations, discrepancies in chord and twist distribution between the tabulated description and CAD model of the rotor were identified. The tabulated data, representing the intended design, was employed in both the GH and previous UoO Blade Element Momentum models. The CAD model, representing the realised design, was used for both the EDF experiments and the UoO blade-resolved simulations. The differences in

geometry have been corrected for the present RANS-BEM simulations by interrogating the CAD model to produce a new tabulated blade description.

Both rotor models, blade resolved and RANS-BEM, produce good agreement with experimental results for power and stream-wise thrust coefficients for the higher flow speeds ($U_{0.5}$, U_1).

Coefficients of power and stream-wise thrust are found not to be sensitive to the free surface modelling technique, whether rigid lid or volume of fluid.

The numerical simulation stencil is tabulated in Section 3.3. Comparisons of a selection of these results with experimental data are presented for a number of cases in the Appendix: stream-wise velocity along the centreline, vertical and horizontal velocity profiles, and contour maps of stream-wise velocity at a single downstream location. The remaining simulation data is available for download from the PerAWaT SFTP server.

5 References

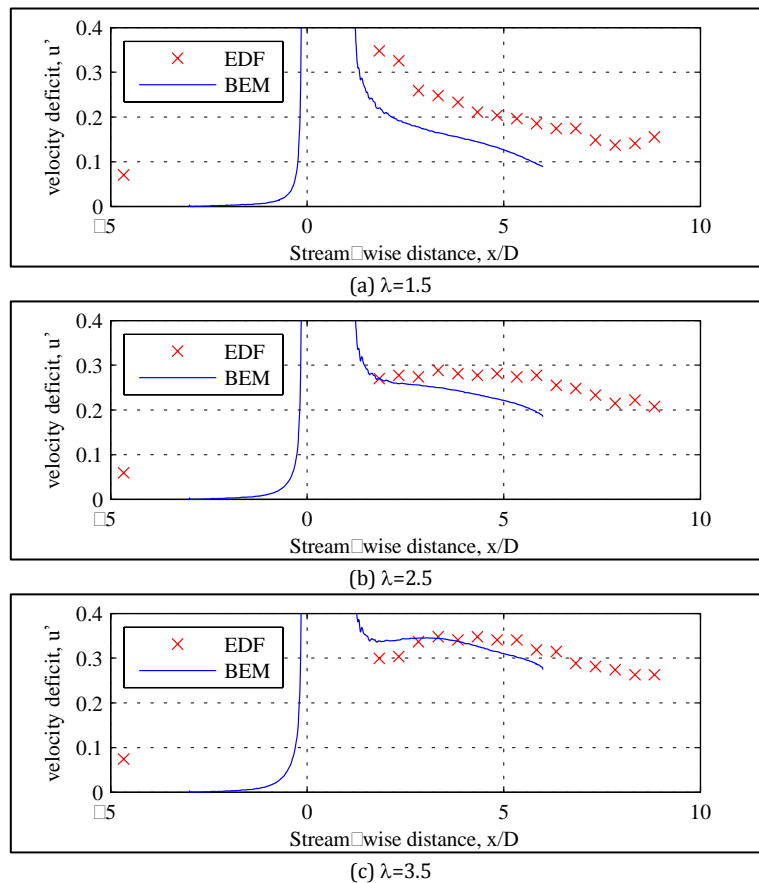
- CONSUL, C.A., WILLDEN, R.H.J. & MCINTOSH, S.C., (2011). An Investigation of the Influence of Free Surface Effects on the Hydrodynamic Performance of Marine Cross-Flow Turbines. In Proc. *EWTEC 2011*, Southampton.
- FLEMING, C.F., MCINTOSH, S.C. & WILLDEN, R.H.J. (2011). WG3 WP1 D2: Report on model setup for ducted horizontal axis axial flow turbines. *Tech Report, PerAWaT project*.
- MCINTOSH, S.C., FLEMING, C.F. & WILLDEN, R.H.J. (2010). WG3 WP1 D1: Report on model setup for horizontal axis axial flow turbines. *Tech Report, PerAWaT project*.
- WHELAN, J.I. (2010). GH Rotor Design - WG4 WP1 D1, 104330/BT/02. *Tech Report, PerAWaT project*.

6 Appendix

6.1 Low Velocity – Low Shear (U0T0)

6.1.1 Centreline Velocity Profile

Experimental velocity deficits are shown in Figure 6.1-1 to exceeded computational values for the lowest tip-speed-ratio ($\lambda=1.5$). With increasing tip-speed-ratio, the initial velocity deficits converge. In both cases a reduction in velocity deficit is seen with increasing streamwise distance. At higher tip-speed-ratios ($\lambda=3.5$ and $\lambda=4.5$) the experimental centreline deficits display an initial increase immediately downstream of the rotor plane. This feature is not captured by the computations.



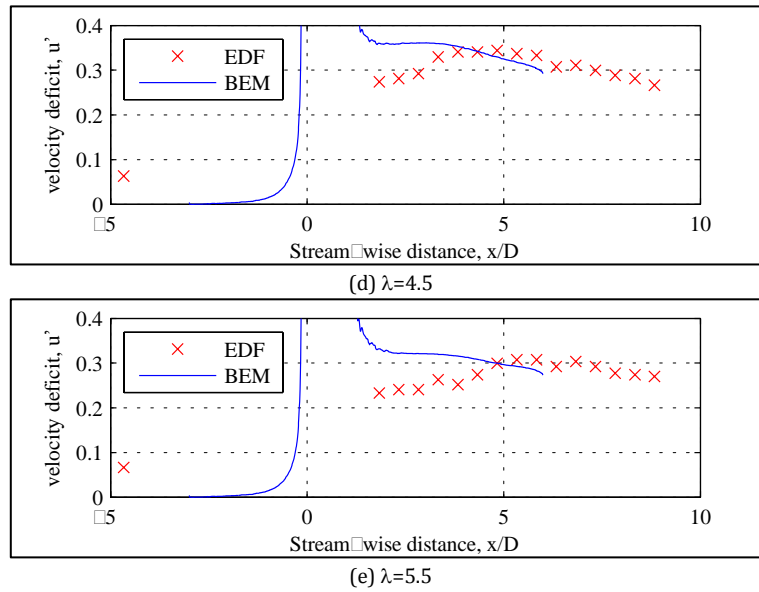
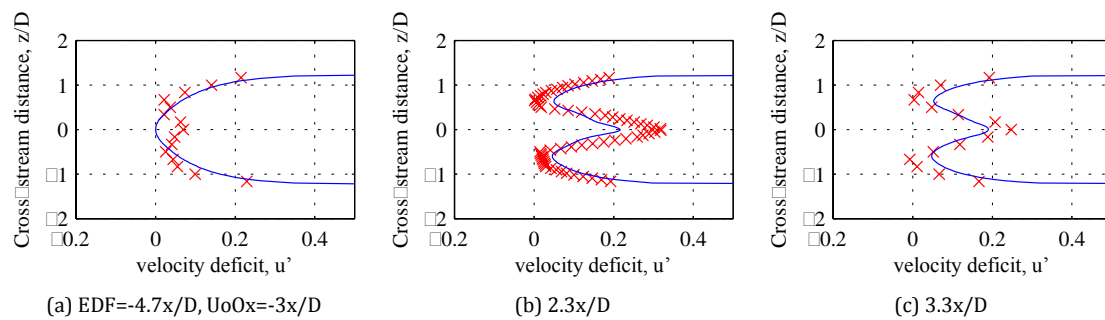


Figure 6.1-1 Centrelines velocity profiles, U0 T0

6.1.2 Horizontal Velocity Profiles

A good agreement is achieved between the experimental and computational cross-stream horizontal profiles for a number of downstream stations. Velocity deficits are shown to be highest along each wall with a smaller central peak due to the turbine (Figure 6.1-2 – Figure 6.1-5). It is suggested here that the unavoidable presence of ‘no-slip’ walls in the EDF experiments, and hence in the UoOx simulations, will contribute to an accelerated wake recovery driven by regions of high shear close to each wall. Good agreement is maintained across the range of tip-speed-ratios studied.



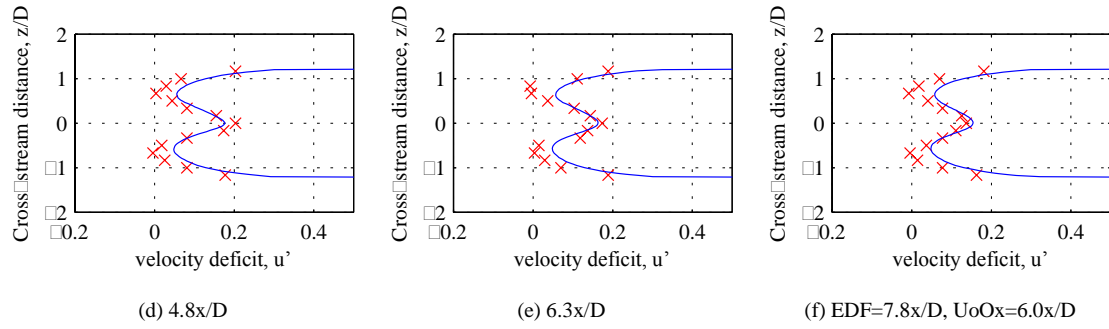


Figure 6.1-2 Horizontal velocity profiles, $\lambda=1.5, U_{O}T_0$

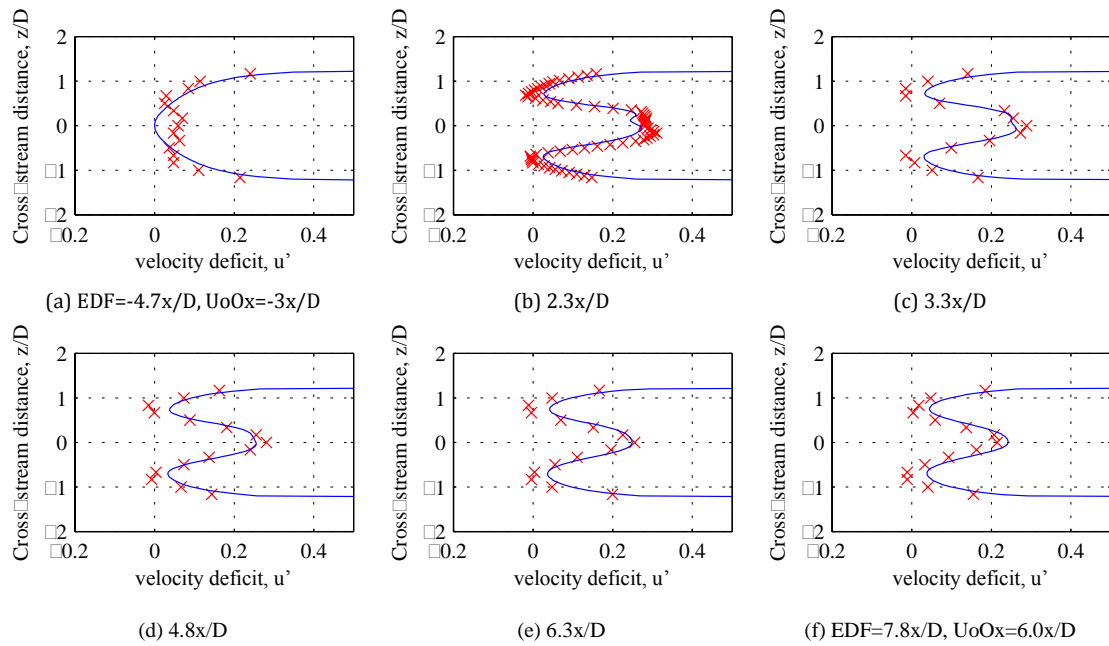
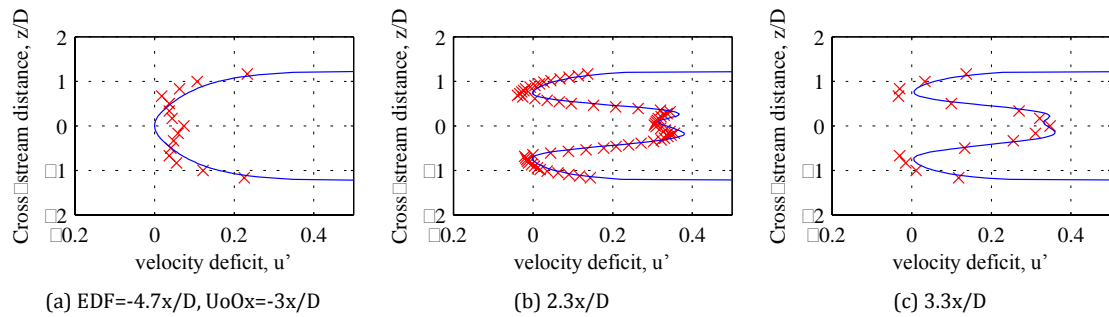


Figure 6.1-3 Horizontal velocity profiles, $\lambda=2.5, U_{O}T_0$



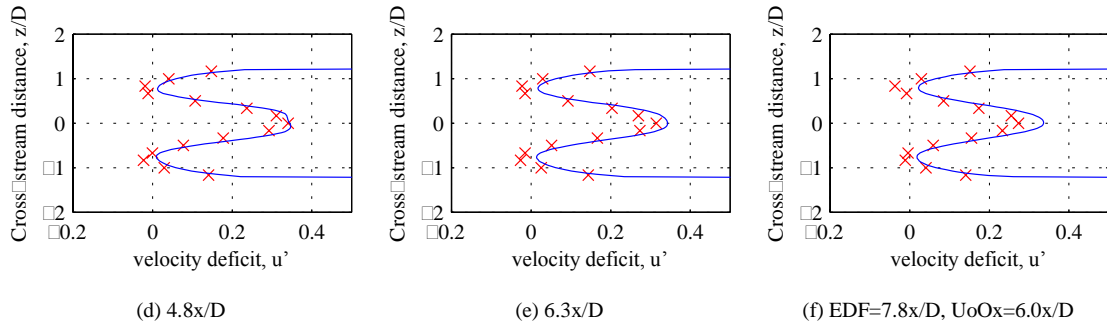


Figure 6.1-4 Horizontal velocity profiles, $\lambda=3.5, U_{0T0}$

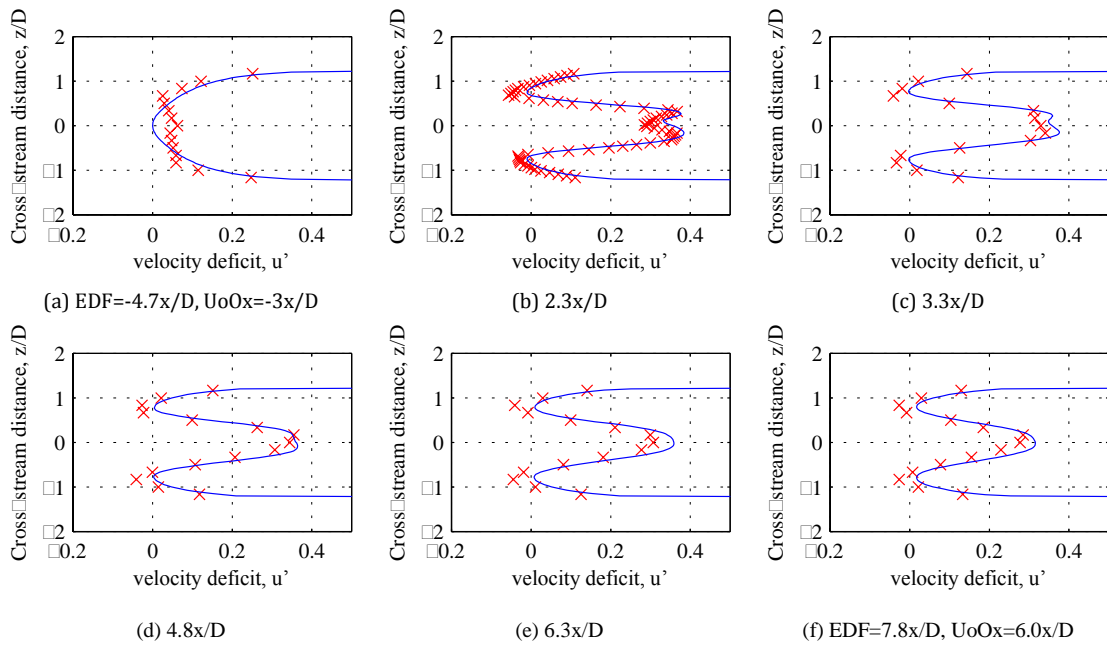
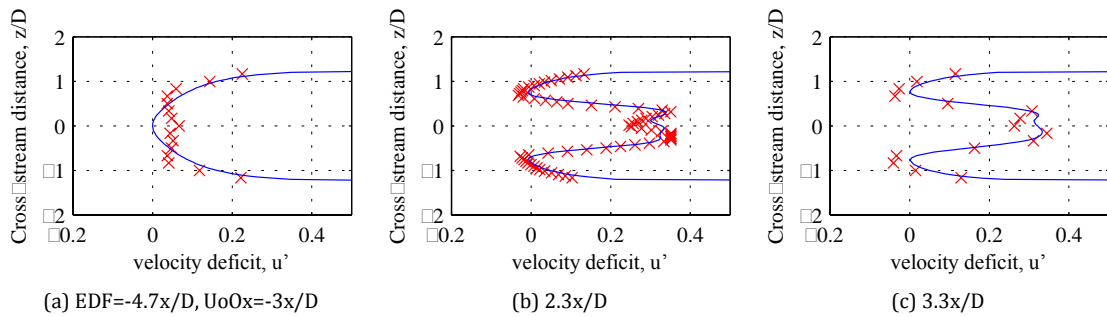


Figure 6.1-5 Horizontal velocity profiles, $\lambda=4.5, U_{0T0}$



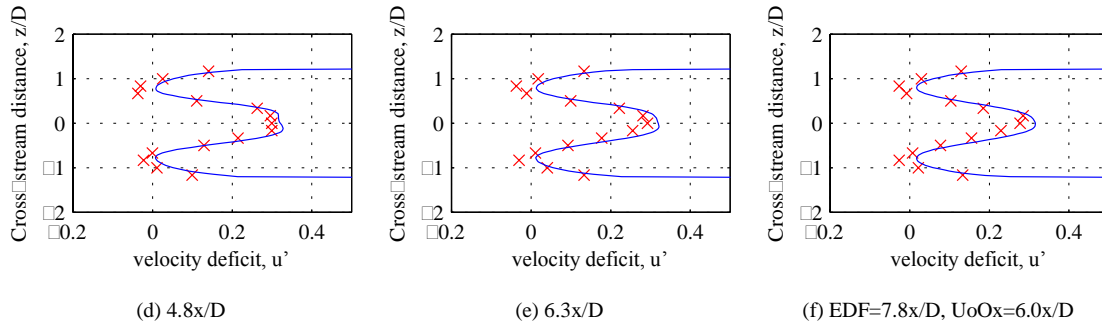


Figure 6.1-6 Horizontal velocity profiles, $\lambda=5.5, U_{0T0}$

6.1.3 Vertical Velocity Profiles

A similar trend, reported for the horizontal profiles, is repeated for the vertical profiles. A good agreement achieved between the experimental and computational results (Figure 6.1-7 –Figure 6.1-11).

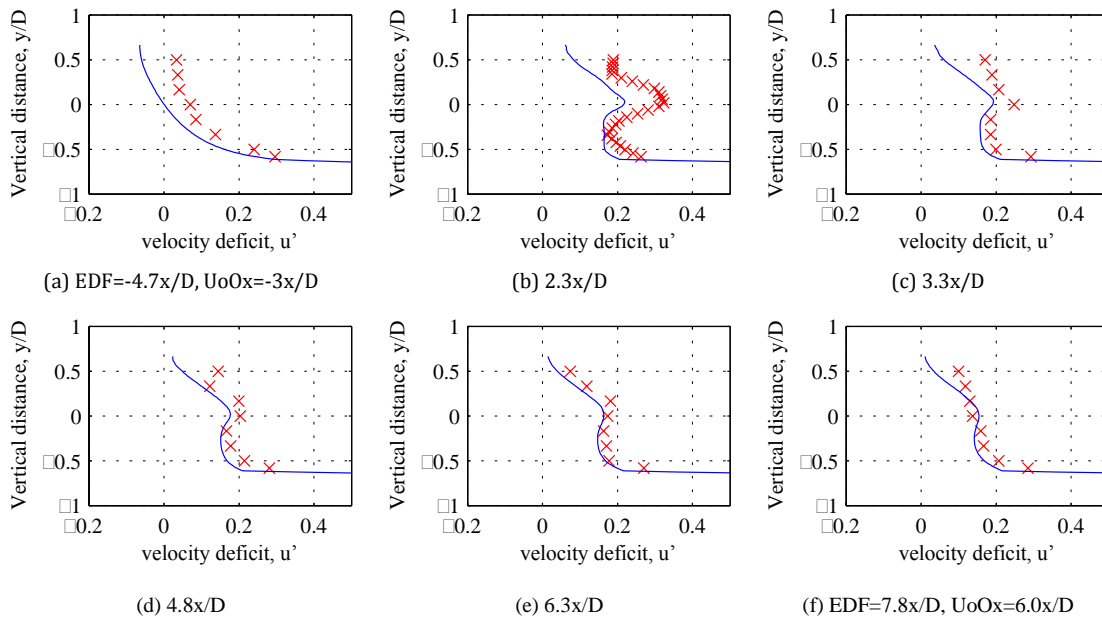
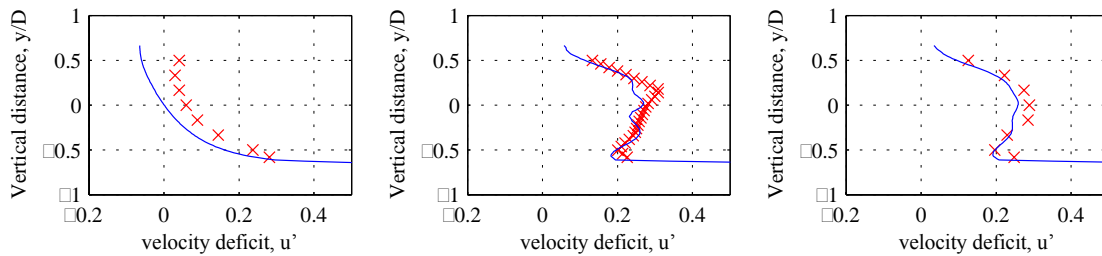


Figure 6.1-7 Vertical velocity profiles, $\lambda=1.5, U_{0T0}$



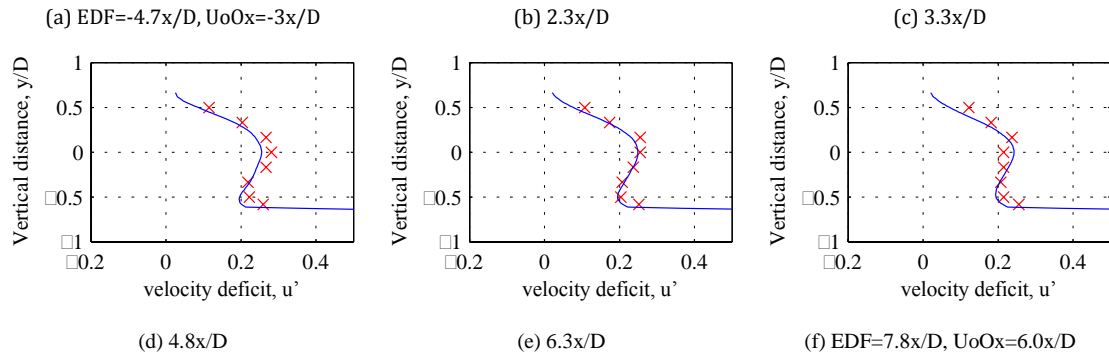


Figure 6.1-8 Vertical velocity profiles, $\lambda=2.5$, U_0T_0

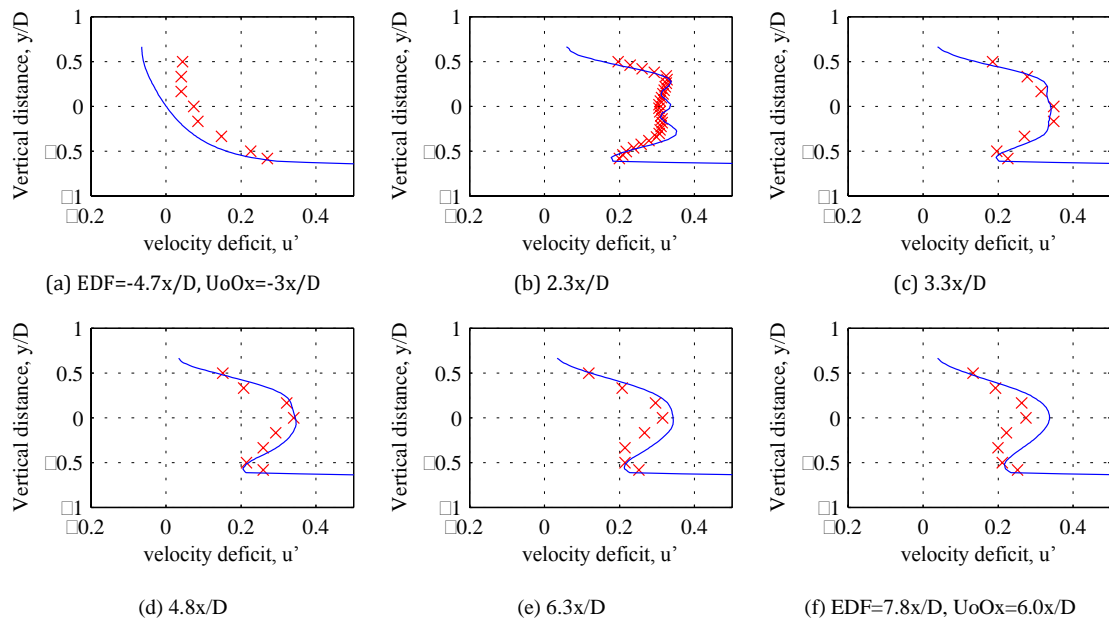
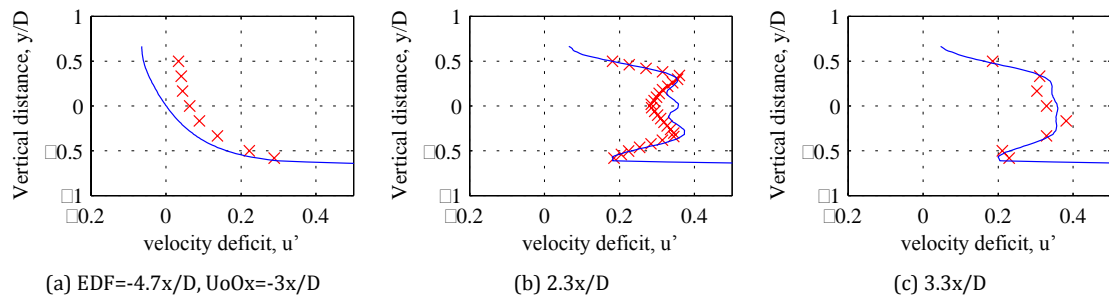


Figure 6.1-9 Vertical velocity profiles, $\lambda=3.5$, U_0T_0



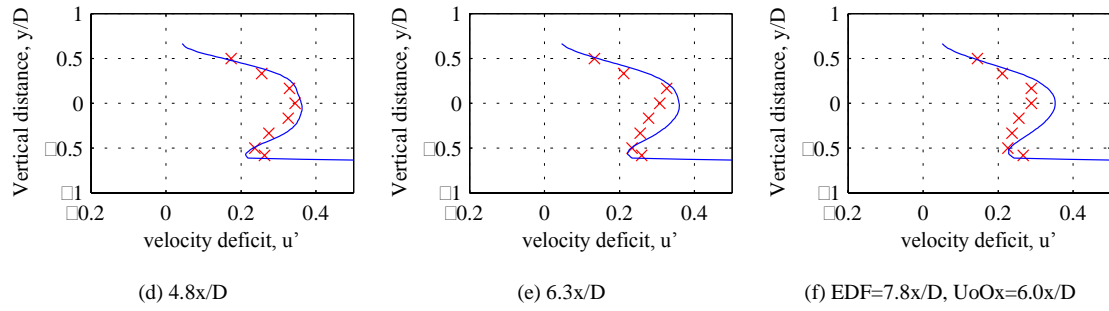


Figure 6.1-10 Vertical velocity profiles, $\lambda=4.5$, U_{0T0}

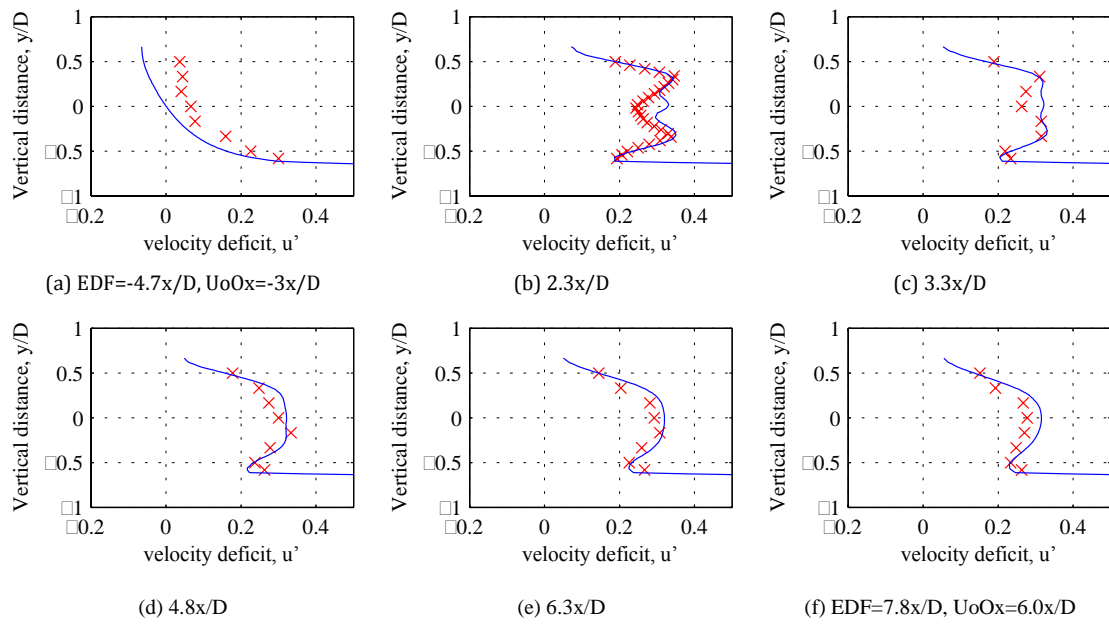
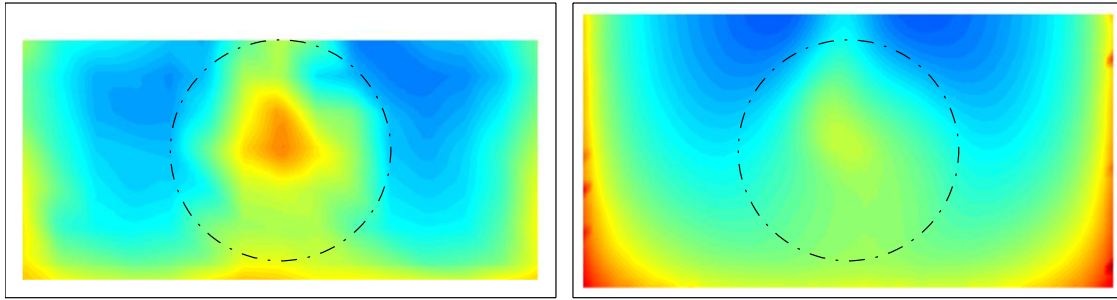


Figure 6.1-11 Vertical velocity profiles, $\lambda=5.5$, U_{0T0}

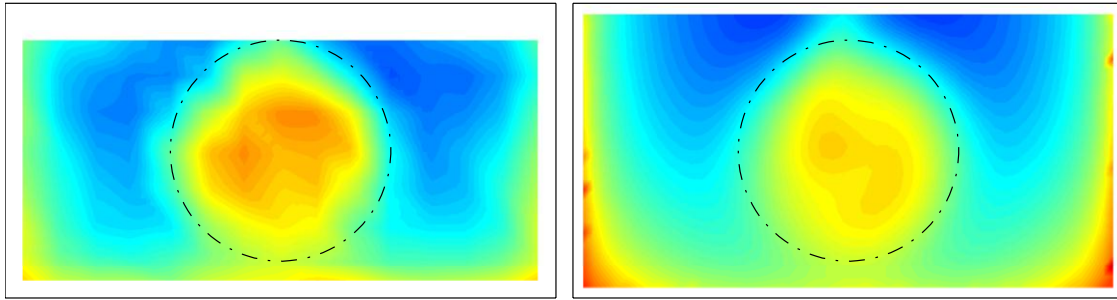
6.1.4 Velocity Grids

A very encouraging comparison is presented in Figure 6.1-12 comparing experimental and computational velocity grids. A high level of agreement is shown both in the magnitude and distribution of the velocity deficit.

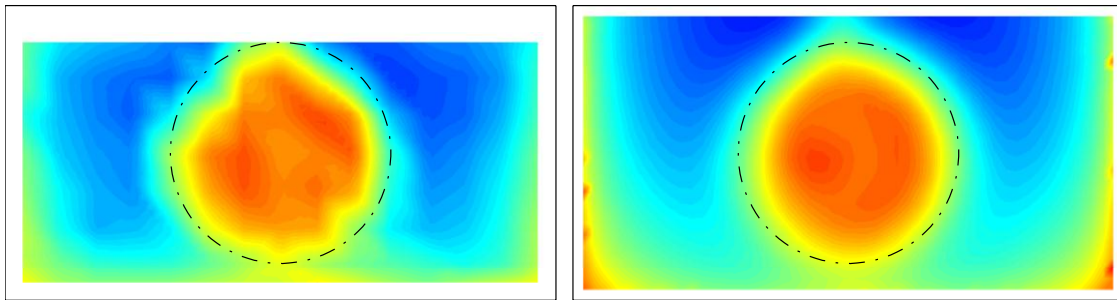
A central region of high velocity deficit, produced by the rotor, is present for all cases. This high deficit region is complemented by negative deficit 'by-pass' flows positioned to each side of the rotor towards the top of the flume. Velocity deficits close to the floor remain high across all tip-speed-ratios studied.



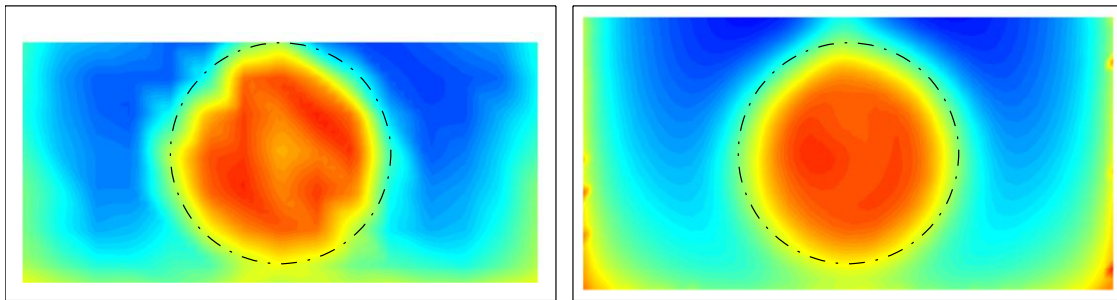
(a) $\lambda=1.5$



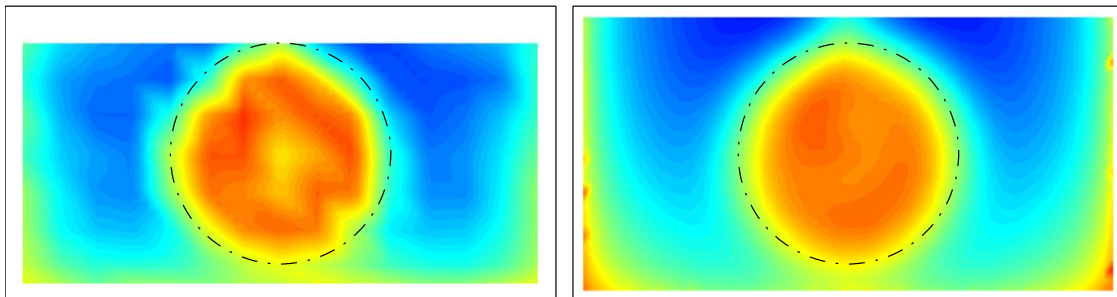
(a) $\lambda=2.5$



(a) $\lambda=3.5$



(a) $\lambda=4.5$



(a) $\lambda=5.5$

Figure 6.1-12 Profiles of stream-wise velocity deficit taken across a plane located 1.4 m downstream of the rotor. Experimental results are in the left hand column, while numerical results are in the right hand column. Colour Scale: -0.2 (blue) - 0.5 (red). Flow Case U0 T0.

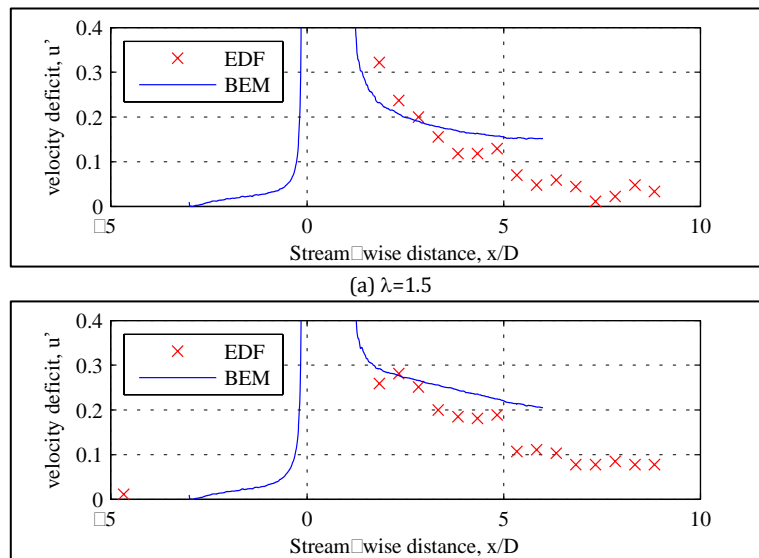
6.2 Low Velocity – High Shear (U0T1)

6.2.1 Centreline Velocity Profile

The centreline profiles for the low velocity high turbulence case, presented in Figure 6.2-1, show a faster recovery of velocity deficit than observed for the low turbulence data set. Here, the velocity deficit is seen to recover to values of $u' < 0.1$ by approximately ten diameters downstream of the rotor plane for the high turbulence case. The low turbulence experiments only achieve a recovery to $u' < 0.3$ over the same distance.

A larger discrepancy between experiment and computation is evident for the low velocity high turbulence data set. Figure 6.2-1 shows a faster recovery of the experimental centrelines. Both experiment and computation follow the same trend of a monotonic deficit reduction with increasing streamwise distance.

The sharp initial increase in velocity deficit immediately downstream of the rotor plane evident in the low turbulence experiments (Figure 6.1-1) is not visible in either the experimental or computational data sets for the low velocity, high turbulence flow case.



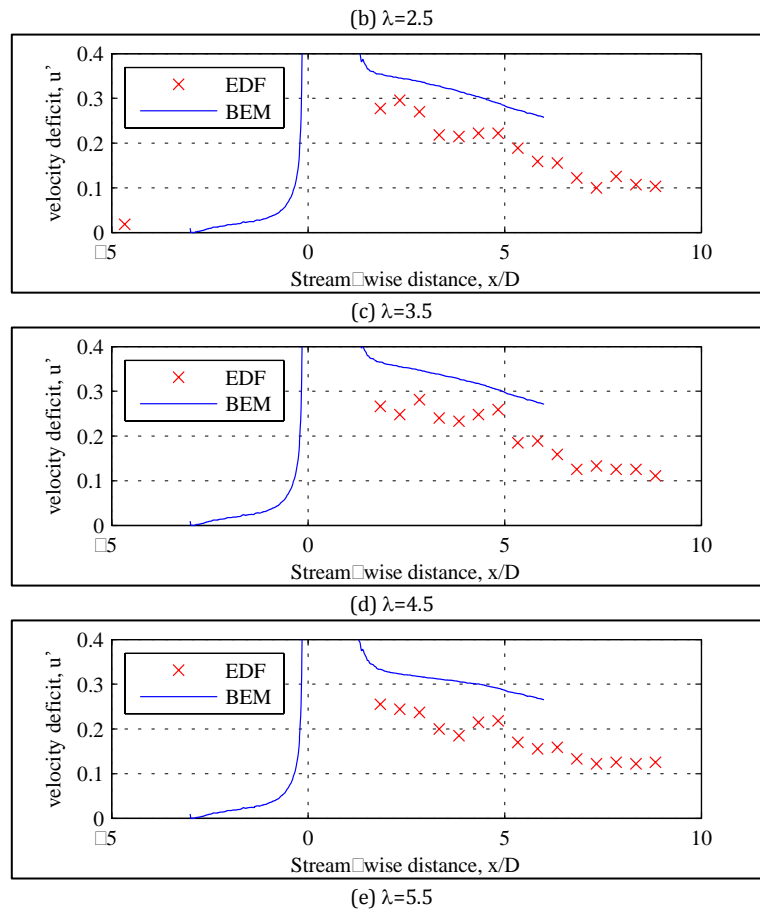
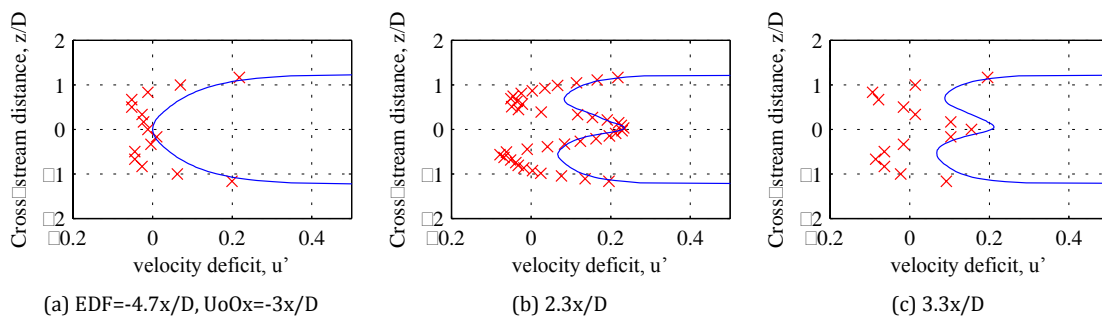


Figure 6.2-1 Centreline velocity profiles, U0 T1

6.2.2 Horizontal Velocity Profiles

Cross-stream agreement between experiment and computational velocity deficits is shown to be less favourable than that demonstrated for the low turbulence case. Figure 6.2-2 – Figure 6.2-6 show a faster wake recovery for the experimental data set than observed in the computations. It is suggested that a combination of discrete structure combined with corner flows not present in the computational model are responsible for the apparent miss-match in velocity deficits.



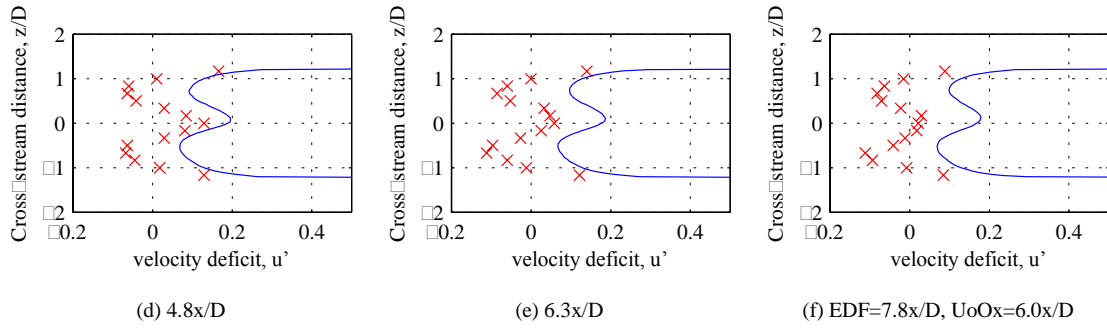


Figure 6.2-2 Horizontal velocity profiles, $\lambda=1.5, U_{0T1}$

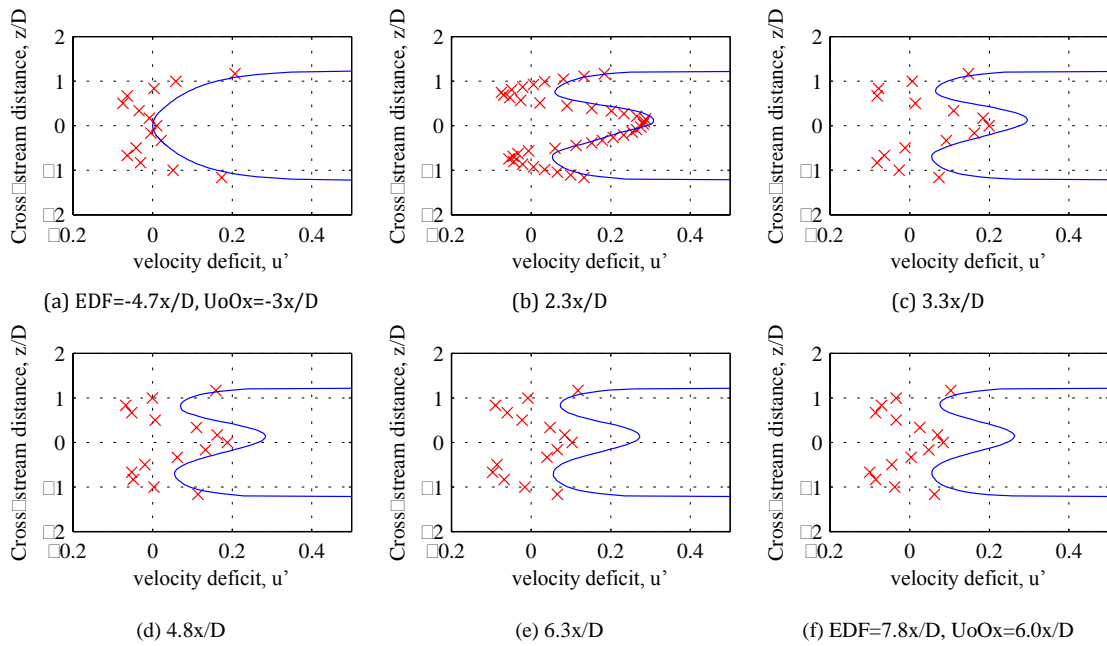
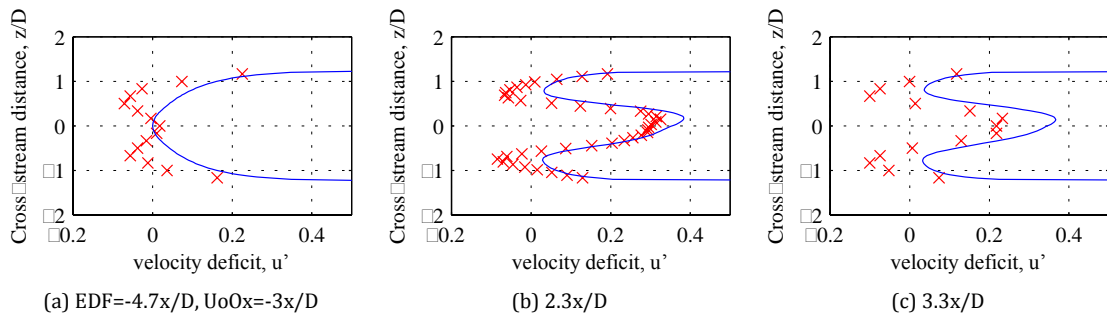


Figure 6.2-3 Horizontal velocity profiles, $\lambda=2.5, U_{0T1}$



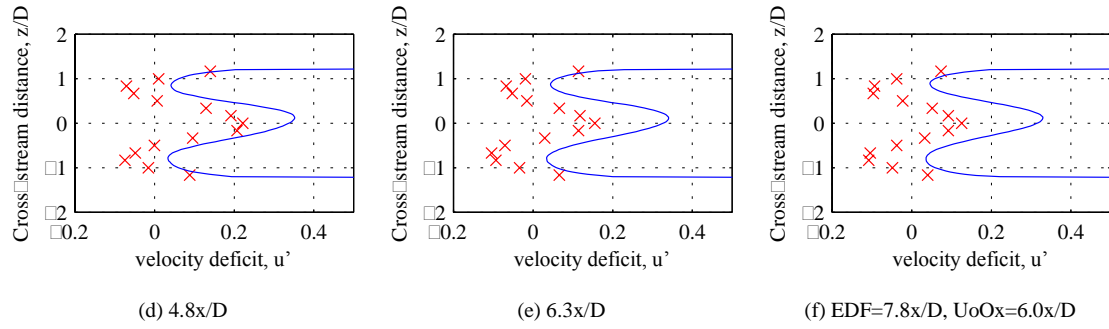


Figure 6.2-4 Horizontal velocity profiles, $\lambda=3.5, U0T1$

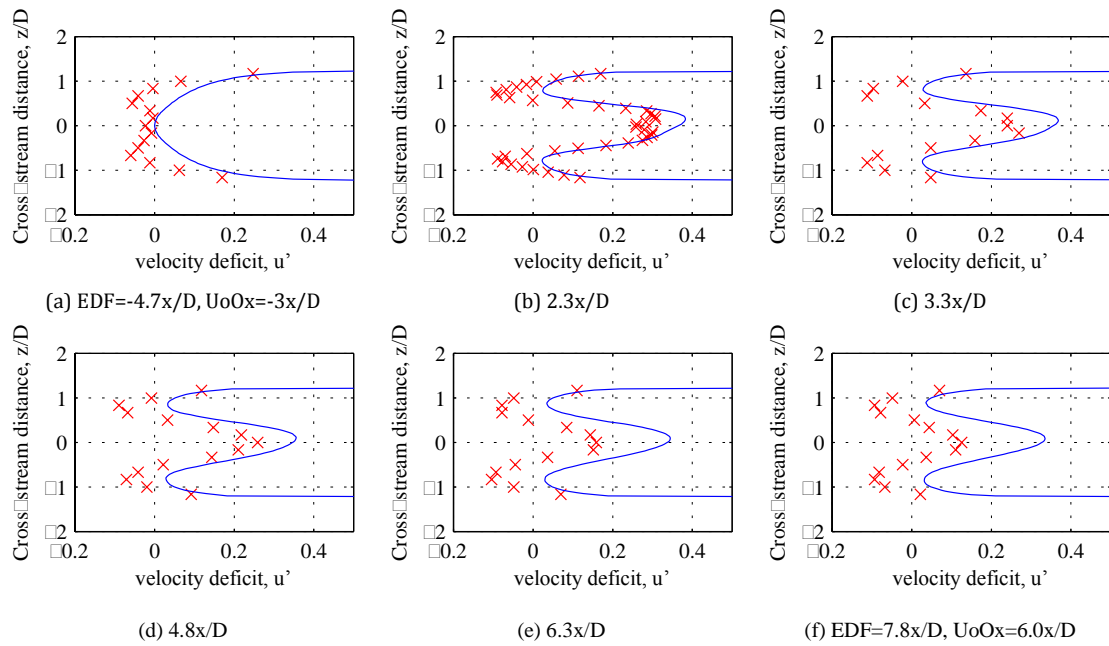
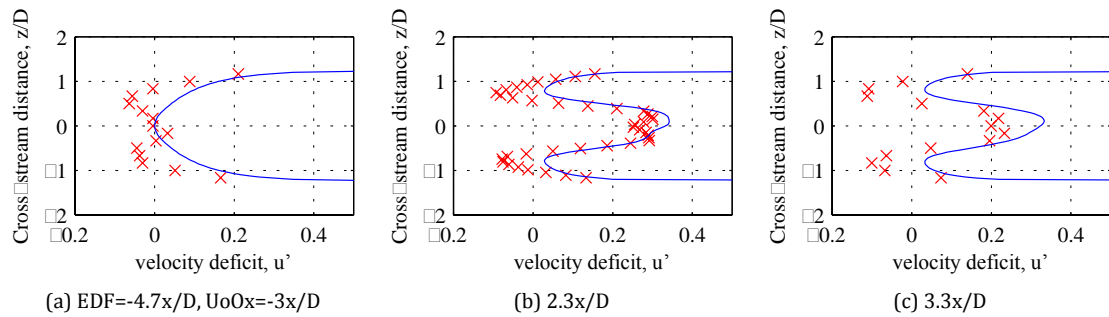


Figure 6.2-5 Horizontal velocity profiles, $\lambda=4.5, U0T1$



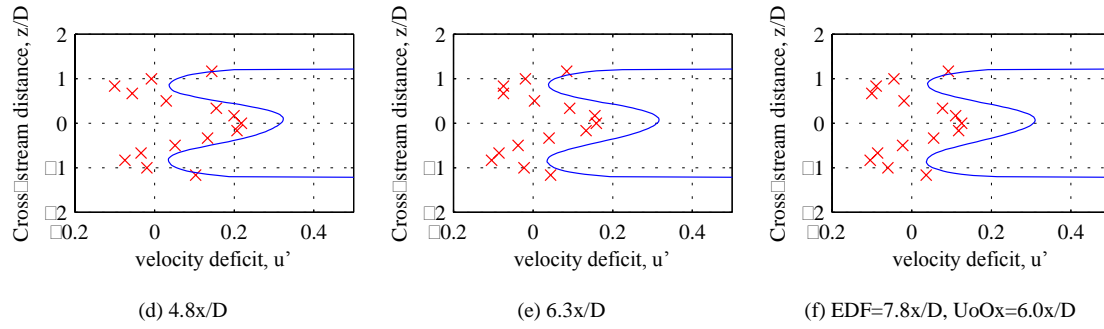


Figure 6.2-6 Horizontal velocity profiles, $\lambda=5.5$, U0T1

6.2.3 Vertical Velocity Profiles

Comparison of the experimental and computational profiles in the vertical direction is shown in Figure 6.2-7 –Figure 6.2-11. Agreement is shown to be good close the top of the flume with the profiles diverging as the floor is approached.

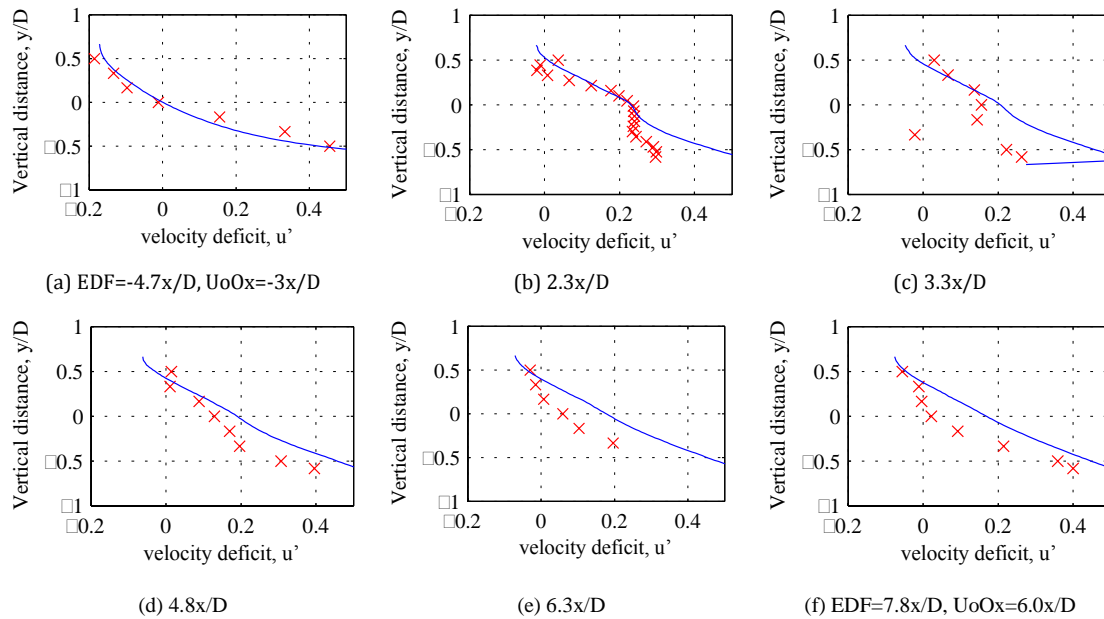


Figure 6.2-7 Vertical velocity profiles, $\lambda=1.5$, U0T1

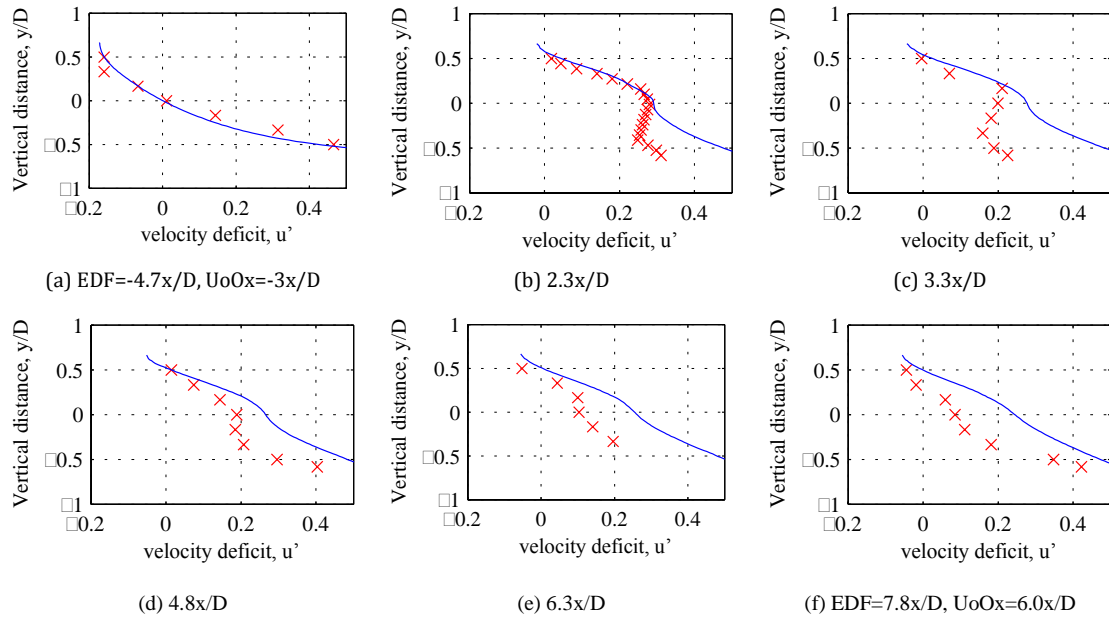


Figure 6.2-8 Vertical velocity profiles, $\lambda=2.5$, U_0T_1

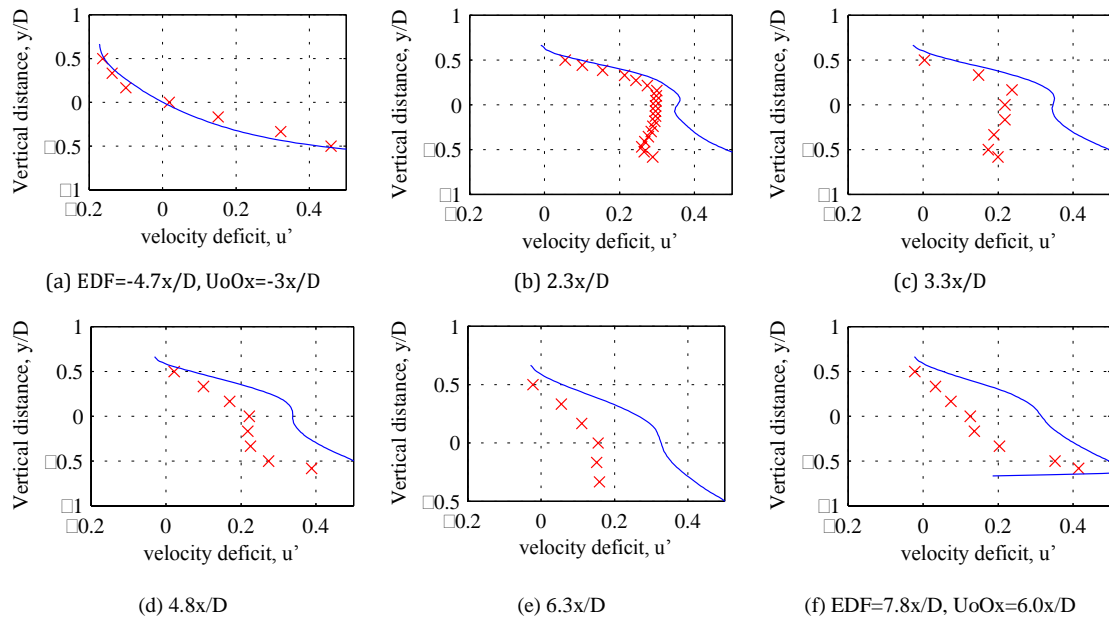


Figure 6.2-9 Vertical velocity profiles, $\lambda=3.5$, U_0T_1

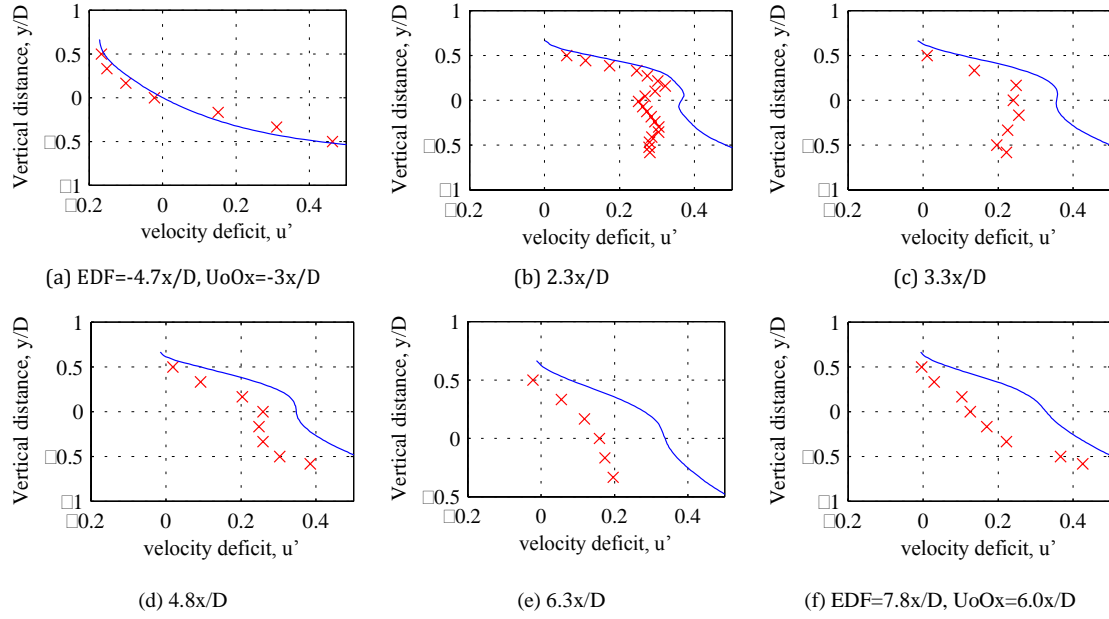


Figure 6.2-10 Vertical velocity profiles, $\lambda=4.5$, U_0T1

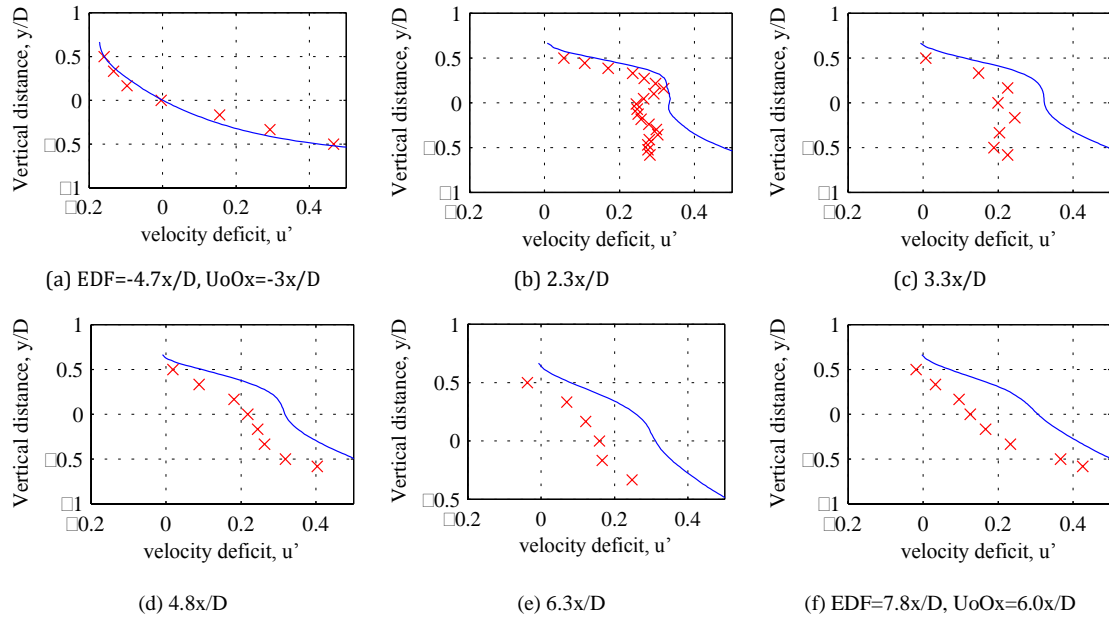
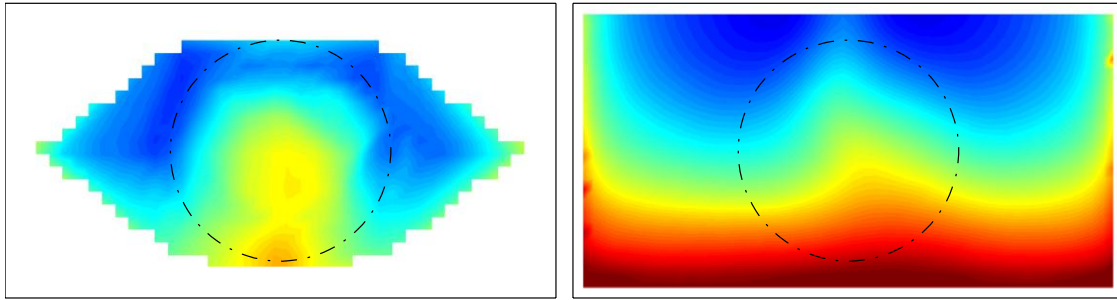


Figure 6.2-11 Vertical velocity profiles, $\lambda=5.5$, U_0T1

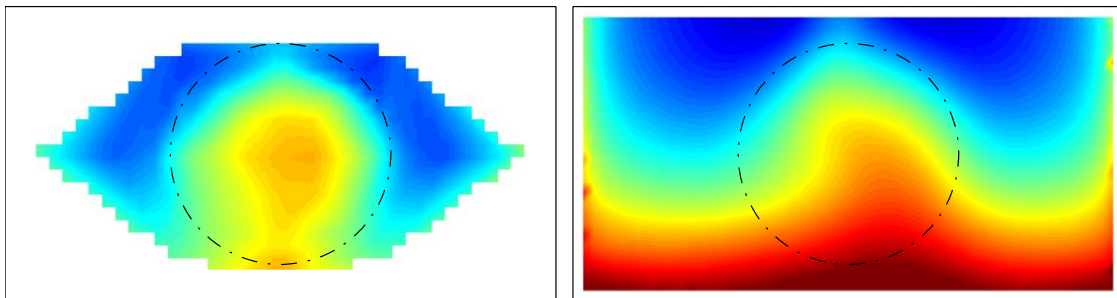
6.2.4 Velocity Grids

The central agreement between the velocity deficit fields shown in Figure 6.2-12 is fair. The vertically sheared velocity profile is evident in both cases. Also evident is an accelerated bypass flow located either side of the rotor towards the

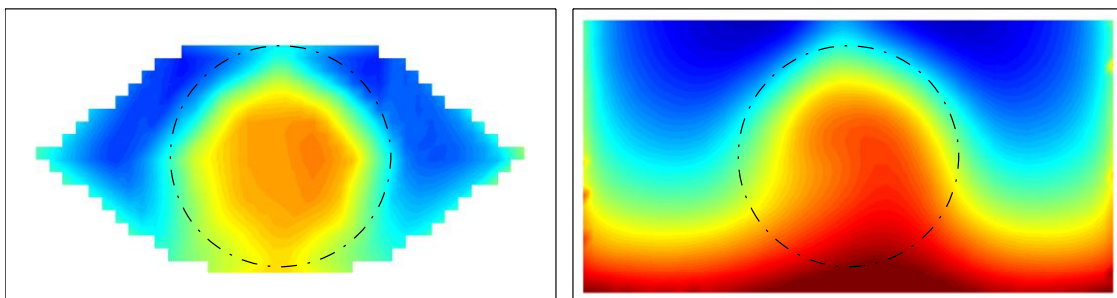
top of the flume that is well captured by both experiment and computation.



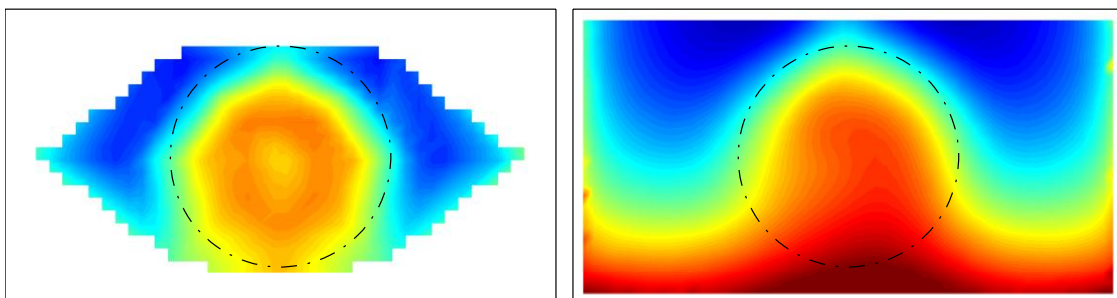
(a) $\lambda=1.5$



(a) $\lambda=2.5$



(a) $\lambda=3.5$



(a) $\lambda=4.5$

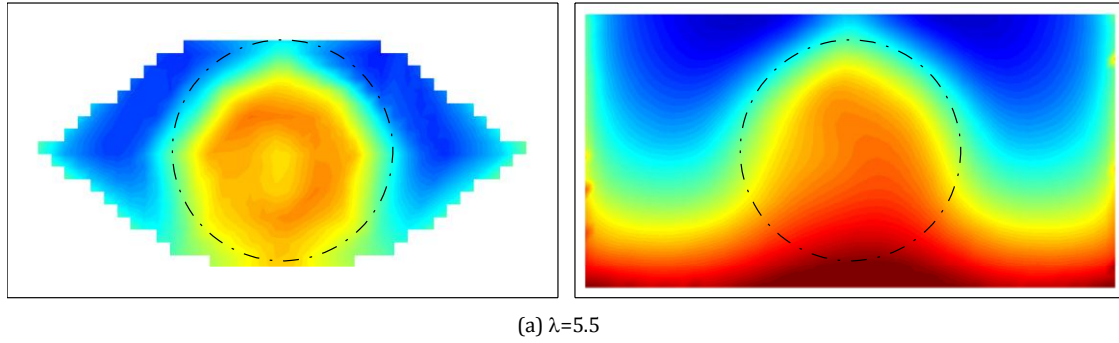


Figure 6.2-12 Profiles of stream-wise velocity deficit taken across a plane located 1.4 m downstream of the rotor. Experimental results are in the left hand column, while numerical results are in the right hand column. Colour Scale: -0.2 (blue) - 0.5 (red). Flow Case U0 T1.

6.3 High Velocity – Low Shear (U1T0)

6.3.1 Centreline Velocity Profile

The high velocity, low shear experiment follows a very similar format to the low velocity, low shear cases discussed in Section 6.1. Centreline velocity deficits both show a steady recovery for streamwise distances greater than 5 diameters (Figure 6.3-1). At closer streamwise stations a sharp increase in velocity deficit is observed in the experimental data, which is not evident in the computations.

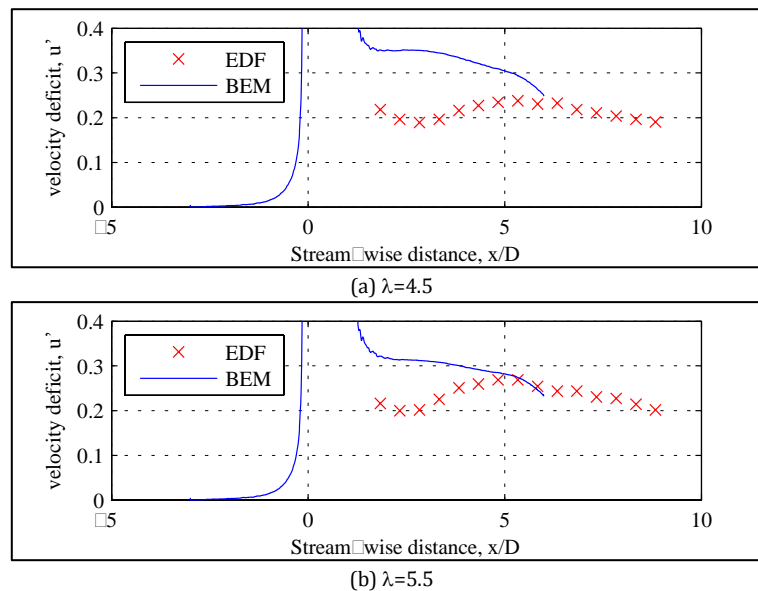


Figure 6.3-1 Centreline velocity profiles, U1 T0

6.3.2 Horizontal Velocity Profiles

A fair agreement is achieved between the horizontal velocity profiles (Figure 6.3-2 – Figure 6.3-3). Large disagreement between inflow profiles (Figure 6.3-2a) is suggested as cause of the offset between the experimental and computational traces.

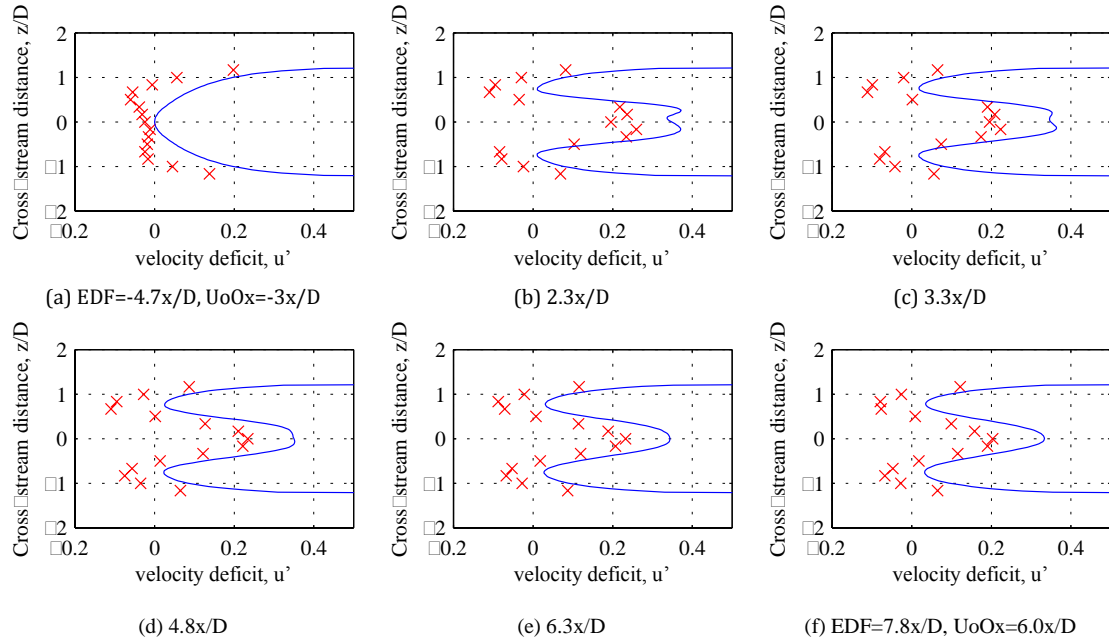


Figure 6.3-2 Horizontal velocity profiles, $\lambda=4.5$, $U1T0$

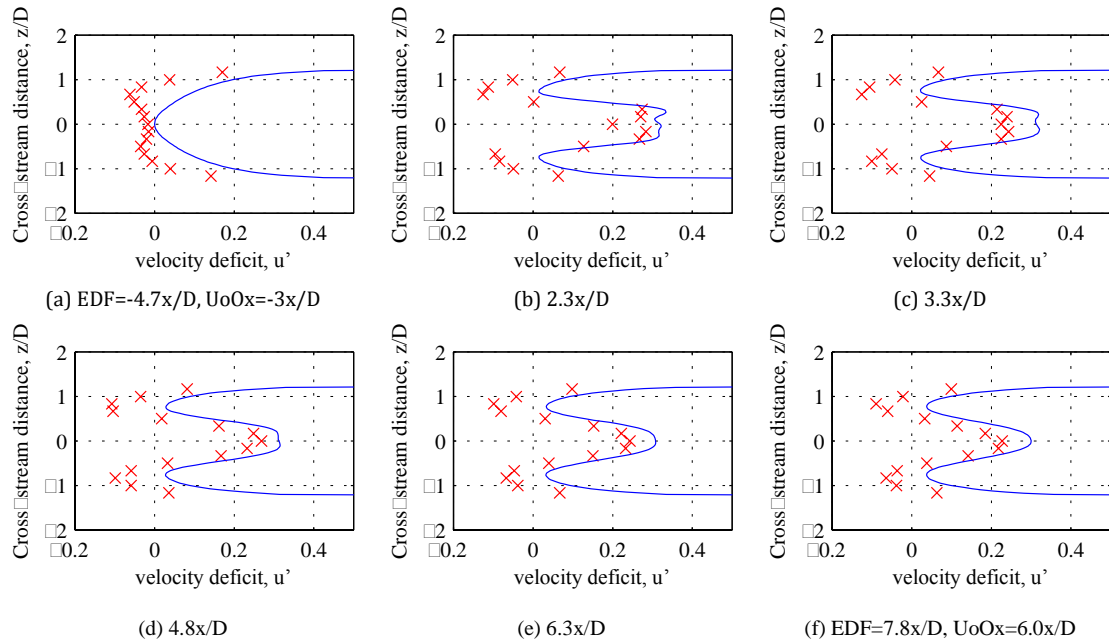


Figure 6.3-3 Horizontal velocity profiles, $\lambda=5.5$, U1T0

6.3.3 Vertical Velocity Profiles

A much better agreement is achieved for the upstream inflow profiles (Figure 6.3-4a). However, cross stream variation of the inflow shown in Section 6.3.2 is the likely cause of subsequent disagreement between the profiles.

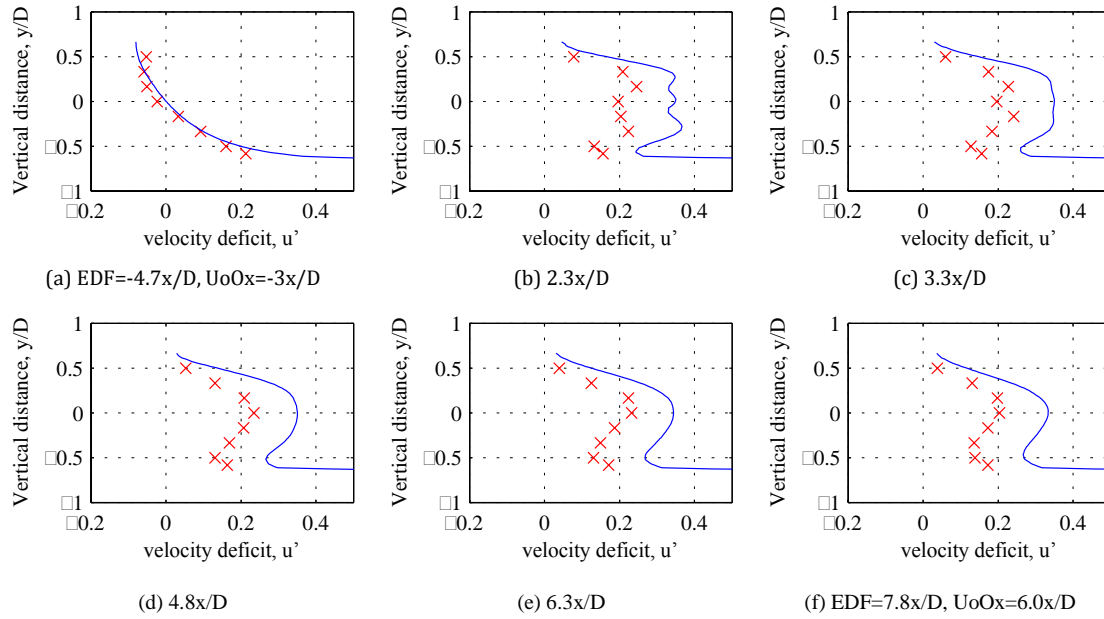


Figure 6.3-4 Vertical velocity profiles, $\lambda=4.5$, U1T0

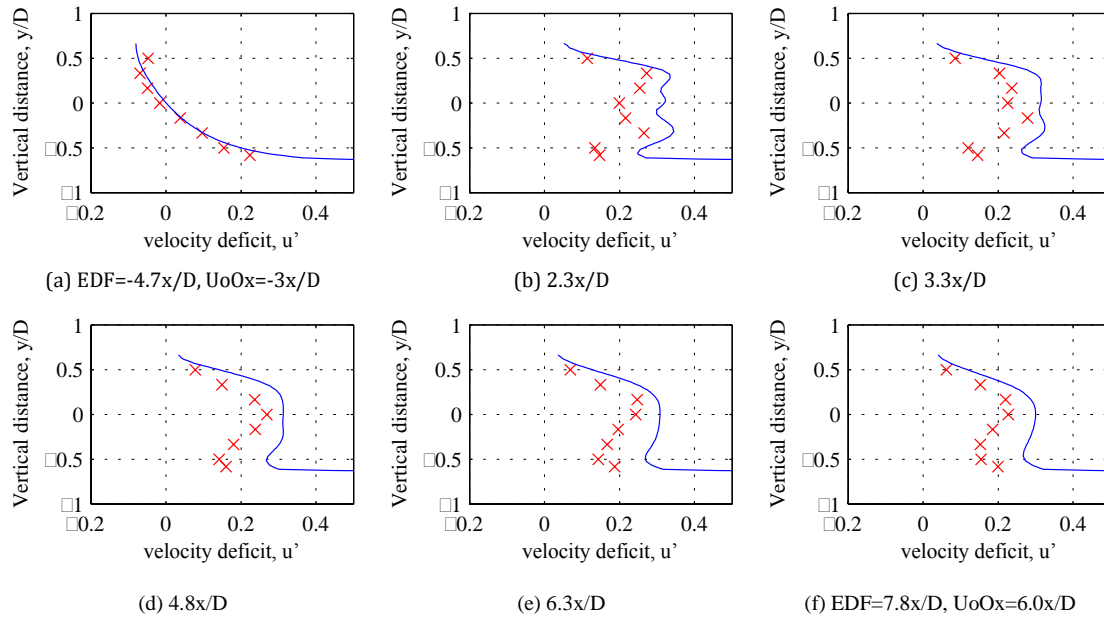


Figure 6.3-5 Vertical velocity profiles, $\lambda=5.5$, U1T0